

PAPER

Influence of temperature on magnetorheological fluid properties and damping performance

To cite this article: Ashok Kumar Kariganaur *et al* 2022 *Smart Mater. Struct.* **31** 055018

View the [article online](#) for updates and enhancements.

You may also like

- [The development of an outer multi-pole magneto-rheological damper with high dynamic range of damping force](#)
Shaogang Liu, Lifeng Feng, Dan Zhao et al.

- [Seismic performance of magnetorheological damped structures with different MR fluid perfusion densities of the damper](#)
Yang Yang, Zhao-Dong Xu and Ying-Qing Guo

- [Development and damping properties of a seismic linear motion damper with MR fluid porous composite rotary brake](#)
Masami Nakano, Jian Yang, Shuaishuai Sun et al.



The advertisement features a large circular logo on the left with the number '250' in red and green, and a blue banner across it reading 'ECS MEETING CELEBRATION'. Below this, text reads: '250th ECS Meeting October 25–29, 2026 Calgary, Canada BMO Center'. On the right, the ECS logo is shown with the text 'The Electrochemical Society Advancing solid state & electrochemical science & technology'. A large white banner says 'Step into the Spotlight'. A red button at the bottom right says 'SUBMIT YOUR ABSTRACT'. At the bottom, a blue banner says 'Submission deadline: March 27, 2026'.

Influence of temperature on magnetorheological fluid properties and damping performance

Ashok Kumar Kariganaur, Hemantha Kumar^{id} and M Arun*^{id}

Department of Mechanical Engineering, National Institute of Technology Surathkal, Mangalore, Karnataka, India

E-mail: m.arun1978@gmail.com

Received 31 December 2021, revised 8 March 2022

Accepted for publication 24 March 2022

Published 13 April 2022



Abstract

The magnetorheological (MR) system's performance depends on the MR fluid's temperature in operation. This study aims to evaluate the temperature effect of MR fluid on performance while the damper is working. Before synthesizing MR fluid, scanning electron microscopy, x-ray diffraction, and particle size analysis verifies for the synthesis of MR fluid in-house.

Characterization of the MR fluid at different temperatures and magnetic fields was carried out. The Herschel–Bulkley model is used to analyse the nonlinearity in the fluid by incorporating the temperature effect. The range of critical parameters used to fabricate the MR damper is selected using the Technique for Order of Preference by Similarity to Ideal Solution performance score. The temperature of the MR fluid is measured using an embedded thermocouple while the damper is operating at different loading parameters. The results reveal that the fluid temperature rises significantly from atmospheric to 125.39 °C with decrease in damping force by 66.32% at higher loading parameters. The theoretical model predicts the increase in temperature similar to that of the experimental values with an average error of 10.24% in the on-state condition. Particle characterization after dynamic testing reveals particle morphology has not changed but the saturation magnetization of the particles reduced by 57% at higher temperatures (127 °C). It is observed through thermogravimetric analysis that, the life of the fluid is reduced by 0.25%, which is negligible after dynamic testing of the fluid for approximately 85000 cycles. Finally, to imitate the temperature effect on the particle, particles were heat-treated at 200 °C, 400 °C, and 600 °C, and through scanning electron microscope image it is confirmed that deterioration of the particle starts after 200°C, if the fluid is operated for a prolonged amount of time.

Keywords: magnetorheological fluids, temperature stability, HB model, magnetorheological damper, SEM, TGA

(Some figures may appear in colour only in the online journal)

1. Introduction

The fluid whose properties change with external magnetic fields is called magnetorheological (MR) fluids, a sub-branch of smart materials. These smart fluids are used in the design and manufacturing of dampers, brakes, clutches for vibration

mitigation, and torque transmission through a control mechanism. Generally, MR fluids consist of magnetic particles which vary in size from 1 to 10 μm [1, 2], a dielectric carrier fluid, and some additives by supplying external magnetic field the fluid becomes semi-solid like increasing the yield stress, with the intensity of the external magnetic field various physical systems such as brakes, clutches, and MR dampers can be controlled to absorb the vibrations. MR fluid-based systems decrease vibrations produced in a mechanical system [3].

* Author to whom any correspondence should be addressed.

The primary concern of the MR fluids is sedimentation stability which is generally a phenomenon happening in MR fluids while systems are stationary, and some researchers have shown that increasing stirring time, stirring speed, increasing the mass fraction of particles with a coating of various single and multiple additives, and using high viscosity carrier fluid sedimentation can be minimized in MR fluid [4–8]. Among the additives, hydrophobic fumed silica with a large particle size gives less viscosity, higher yield stress, and a better recovery rate than hydrophilic fumed silica [9, 10]. Moreover, physical parameters of magnetic particles such as shape, size, concentrations, and particles with bidisperse in form and magnetic saturation play an essential role in sedimentation and flow characteristics variation of the MR fluids [11–13]. Typically, octahedral-shaped and plate-like micro-sized magnetic particles with single-walled nanotube particles and fumed silica additive increases sedimentation time, dynamic yield stress, viscosity, and sedimentation stability [14–17]. Researchers have shown experimentally that temperature significantly influences sedimentation [18]. It was proposed that particle size and high particle concentration can induce wear on the surface, and yield stress can be increased by applying external compression load and magnetic field on the fluid [19, 20]. The shear-thinning effect with a decrease in yield due to magnetic saturation can be observed at higher magnetic field strengths [21, 22]. The dispersion stability of the magnetic particles can be improved by incorporating organo-clay as an additive, and further increasing the additive reduces yield stress of the fluid [23, 24]. However, the temperature has a significant effect on the properties of the MR fluid; experimentally, it was revealed that yield stress of the MR greases decreases with an increase in applied magnetic field and temperature [25]. The viscosity and dynamic yield stress due to thermal expansion of the fluid had been captured using constitutive models and taking temperature and magnetic field into account [26, 27]. For the temperature effect to overcome thermoresponsive carrier fluid is used where sol-gel is formed, increasing the stability with reduced degradation time [28–30]. Experimentally it is shown that testing of MR fluid for durability shows an increase in temperature with a decrease in viscosity and yield stress [31].

Due to its variability and controlling capability, MR fluid systems can be widely used in many applications, and one of them is MR damper, and it is used to remove the undesirable vibrations from the systems for better performance. Material properties of the damper and fluid flow gap are the essential parameters in the design of the MR damper and optimization through finite element (FE) analysis [32–34]. FE modelling and computational fluid dynamics (CFD) are used to obtain the maximum flux density. Researchers showed that the better output could be obtained by giving weights to individual parameters using the technique for order of preference by similarity to the ideal solution [35, 36]. It is confirmed from the literature that temperature sensitivity is to be considered in designing the damper to enhance its effectiveness [37]. In addition, optimal parameters such as gap, current, and particle

concentration are obtained for the design of the MR damper through the response surface method [38–40]. The thermal conductivity of the MR fluids can be increased by increasing the particle concentrations and magnetic field [41, 42]. Finite analysis shows us that the piston rod dimension plays a significant role in distributing the magnetic flux to the gap and is studied through experimentation in twin-tube bypass, which gives higher damping force and can operate in fail-safe. A way to calculate the damping force of the damper is obtained through repeated experimentation and curve fit analysis [43–45]. The optimal parameters were obtained through the FE method and ANSYS parametric design language. The damping force can be enhanced by increasing the applied current [46, 47]. The double tube MR damper model in MATLAB/Simulink is used to study the effect of parallel plate and gap between the gap plates affects fluid flow [48]. Heat generation inside the damper makes the liquid temperature rise, decreasing the fluid's viscosity, reducing the MR damper's performance [49]. The design process minimized temperature rise by implementing the six sigma algorithm [50]. Therefore, it is necessary to fabricate the damper, giving feasible geometric dimensions to measure the fluid temperature inside the damper while working.

As a whole, the literature study shows the temperature effect on MR fluid properties. However, a survey related to sedimentation rate at different temperatures and flow characteristics with varying temperature and magnetic fields is needed, along with the effect of temperature on the damper's performance while working and assessing the life of the fluid and particle through thermogravimetric analysis (TGA) and scanning electron microscope (SEM) of heat-treated CI particles after dynamic testing of the fluid. Hence an effort was initiated in the present work to study temperature aspects of MR fluid and their performance using a damper.

2. Synthesis of MR fluid

Characterization of magnetic particles and steps to prepare MR fluids are presented in the following section shown in figure 1.

2.1. Particle characterization

Materials used for MR fluid preparation include carbonyl iron (CI) particles (manufacturer: Sigma Aldrich, 44890), lithium grease (manufacturer: Permatex 80345) as an additive, silicone oil (manufacturer: Sigma Aldrich, 378372) as base fluid. SEM and particle size analyser (PSA) were used to obtain the shape (morphology) and average particle diameter of particles, respectively. The crystalline structure is analysed using x-ray diffraction (XRD) at a 2° min^{-1} scanning rate with radiation of $\lambda = 1.54 \text{ \AA}$. Precision electronic balance for weighing the required quantity of carrier fluid, stabilizer, CI particles, and geared stirrer to disperse the particles in the carrier fluid are the

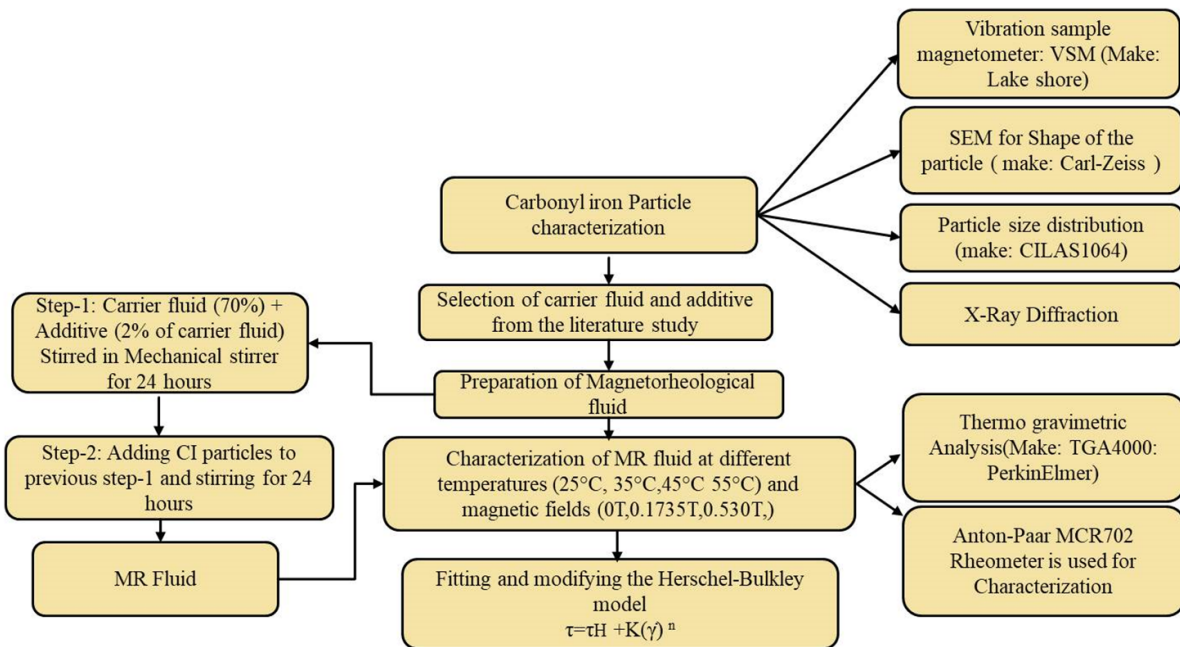


Figure 1. Methodology for particle analysis and characterization of MR fluid.

Table 1. MR fluid components and their properties.

Carbonyl iron powder properties	
Density	7.86 g ml ⁻¹
Shape	Spherical
Size	5–9 microns
Properties of silicone oil	
Viscosity	350 cSt at 25 °C
Density	0.968 g ml ⁻¹
Boiling point	≥140 °C
Properties of lithium base grease	
Viscosity	45 100 cSt at 40 °C
Boiling point	≥250 °C

instruments necessary to prepare the MR fluid. The properties of CI particles provided by the supplier are shown in table 1.

2.2. Synthesis of MR fluid

Table 2 refers to the materials used for MR fluid preparation. First, the silicone oil and stabilizing agent are weighed using the precision weighing balance and then transferred to a beaker. The silicone oil and stabilizer are stirred for about 4 h by setting up the speed of a geared stirrer. Finally, after homogenizing the carrier fluid and stabilizer, CI particles were added to the same beaker and stirred for about 12–14 h at 700 rpm. The volume fraction of silicone oil and CI powder was taken in the ratio of 70% and 30%, respectively. Additives of 2% by volume of silicone oil were added to the carrier fluid. Figure 2 shows us the MR fluid preparation steps. Synthesized MR fluid is further characterized for sedimentation stability and flow behaviour discussed in the following sections.

Table 2. Constituents used for preparing MR fluid.

Materials used	Quantity (volume fraction in %)
Silicone oil	70
Carbonyl iron powder	30
Lithium white grease	2

2.3. Stability of MR fluid

A high density of CI particles is a factor that influences the sedimentation of MR fluids when compared to base fluid density. The particles tend to settle towards the bottom of the measuring cylinder due to gravity, as the particles settle to the bottom, a volume of precise carrier fluid forms at the top of the measuring cylinder. The stability of MR fluid is measured as the ratio of the height of clear fluid after settling to the total volume of the MR fluid filled in the measuring cylinder before settling and is called sedimentation ratio.

Sedimentation ratio(%)

$$= \frac{\text{height of the clear fluid (ml)}}{\text{the total height of the fluid before settling (ml)}} \times 100.$$

The in-house MR fluid is taken in a 10 ml measuring cylinder. The measuring cylinder is provided with graduations of 0.2 ml, as shown in figure 3. The sedimentation is observed by measuring the height of the layer of particles settled with time. Many parameters affect the sedimentation rate, such as carrier fluid viscosity, shape, size of particles, stabiliser added, and carrier fluid temperature. All the parameters were kept constant except the fluid temperature in this work. To vary the temperature of the fluid, incubator is used that has a maximum temperature of 100 °C with 2%–3% error band.

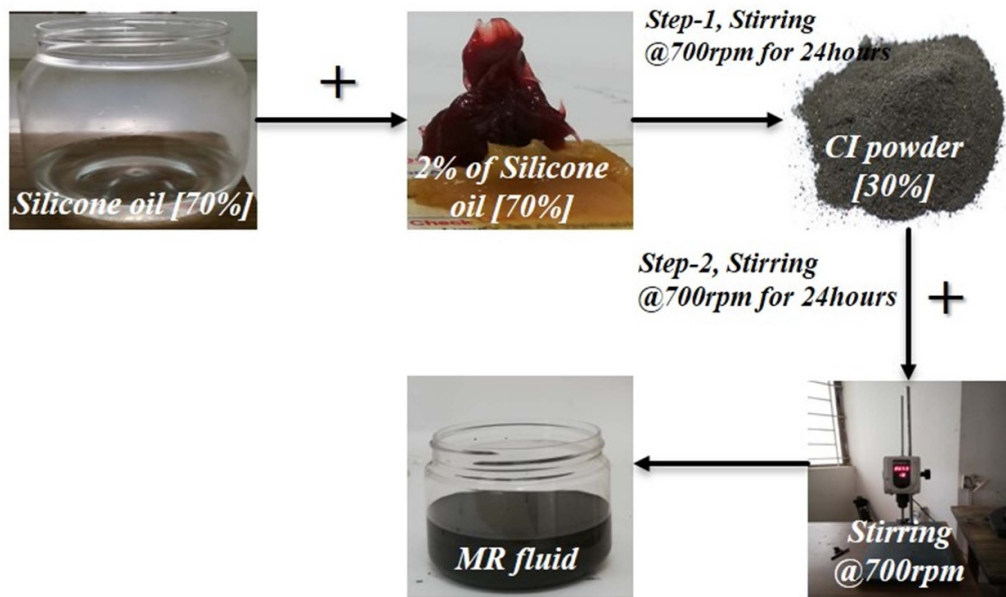


Figure 2. MR fluid synthesis.



Figure 3. MR fluid sample before and after settling.

3. Rheological characterization of in-house MR fluid

Measuring conditions:

- Shear gap = 1 mm
- Shear rate = 0.1–1000 s⁻¹
- Magnetic fields = 0, 0.1735, 0.530, 0.890 T
- Temperature = 25 °C, 35 °C, 45 °C, 55 °C.

MR fluid rheological behaviour has been obtained using a rheometer (make: Anton-Paar MCR 702). The rotational rheometer can provide shear stress and viscosity values at the

required magnetic field and temperatures which is shown in figure 4. Approximately 0.32 ml sample is loaded onto a bottom plate, and the shear gap is maintained at 1 mm between the plates while testing. Obtained values might have an error of ±1%–2% due to sample loading of MR fluids with high viscosity. The rheometer has a temperature control unit that can heat the fluid to a maximum of 70 °C and cool the liquid to ambient temperature.

3.1. Temperature dependence of MR fluid viscosity

Temperature and shear rate significantly influence the viscosity and affect the performance of MR fluid. Therefore, MR fluid viscosity varying with temperature and magnetic field was intended to be studied in the present work. MR fluid behaves as Newtonian fluid in zero magnetic fields, and when the field is applied, it shows a non-Newtonian fluid behaviour. Viscosity curves under the varying shear rates of 0.1–1000 s⁻¹ at required magnetic fields and temperatures are determined.

3.2. MR fluid yield stress

The fluid flow is restricted by CI particles arranged in a chain-like structure in the applied magnetic field, increasing MR fluid's yield point. It is also referred to as the MR effect, and figure 5 represents the schematic representation of the MR effect.

In this section, the behaviour of MR fluid for yield stress with and without magnetic field was studied at different individual temperatures. The shear stress behaviour with varying shear rate is observed at 25 °C, 35 °C, 45 °C and 55 °C temperatures and at constant magnetic fluxes of 0, 0.1735, 0.53 and 0.890 T. Under magnetic fields, yield stress increases at low shear rates compared to high shear rates. The variation in the yield stress with a supply of external magnetic field has

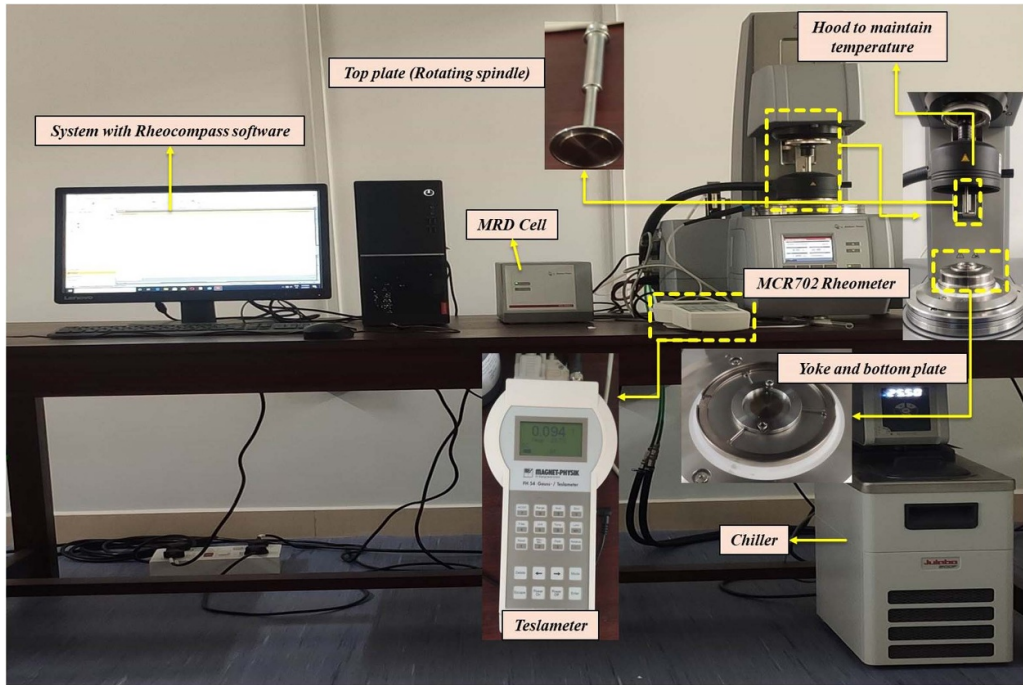


Figure 4. Rheometer for MR fluid property measurements.

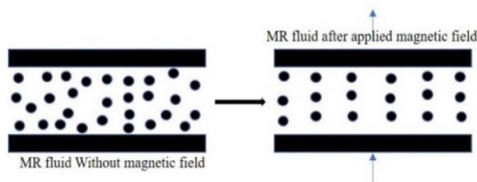


Figure 5. MR effect with the application of external magnetic field.

been modelled based on Herschel–Bulkley (HB) model given by the equation below.

$$\tau = \tau_H + K(\dot{\gamma})^n \quad (1)$$

$$\dot{\gamma} = 0, \tau < \tau_H$$

where τ = shear stress (Pa), τ_H = field (H)-dependent yield stress (Pa), $\dot{\gamma}$ = Shear rate (s^{-1}), K = consistency index and n = flow behaviour index.

4. Design and fabrication of MR damper

This section notes some essential performance parameters from the previous literature review and is optimised using the simple Technique for Order of Preference by Similarity to Ideal Solution (TOPSIS) method for better performance. Following are the vital parameters listed below is considered:

- Fluid flow gap
- Effective pole length
- Core length to accommodate coil turns

- Number of turns of the coil
- Applied current.

Some of the above parameters and their relations were explained in section 4.2. Before going on to the actual fabrication process, the required dimensions have to be selected for the required size according to the raw material available. The material used for fabrication is selected from FE analysis. Externally, the current supplied to the circuit can be controlled, but the other parameters should be decided before fabrication. The size (length, considering the maximum operating amplitude) and piston core must be fixed. Based on the limiting values, optimisation for geometric dimensions was carried out and the methodology for this study is given in figure 6. The primary step in this method is to convert all the parameter values into a normalised matrix using equation (2).

$$r_{ij} = \frac{x_{ij}}{\sqrt{\sum_{i=1}^m x_{ij}^2}}. \quad (2)$$

After selecting normalization weights, find out the weighted normalized matrix by multiplying the equation with weights chosen and given by equation (3).

$$a_{ij} = \omega_j r_{ij}. \quad (3)$$

The next step is to find out the ideal best (B^+ = increasing values among the parameters corresponding to given higher weights) and ideal worst parameters (B = decreasing values among the parameters corresponding to given lesser weights). Here, effective flange length and fluid flow gap are given weightage with 0.1 and 0.2 respectively, core length and a number of coil turns are given 0.1 each, and maximum

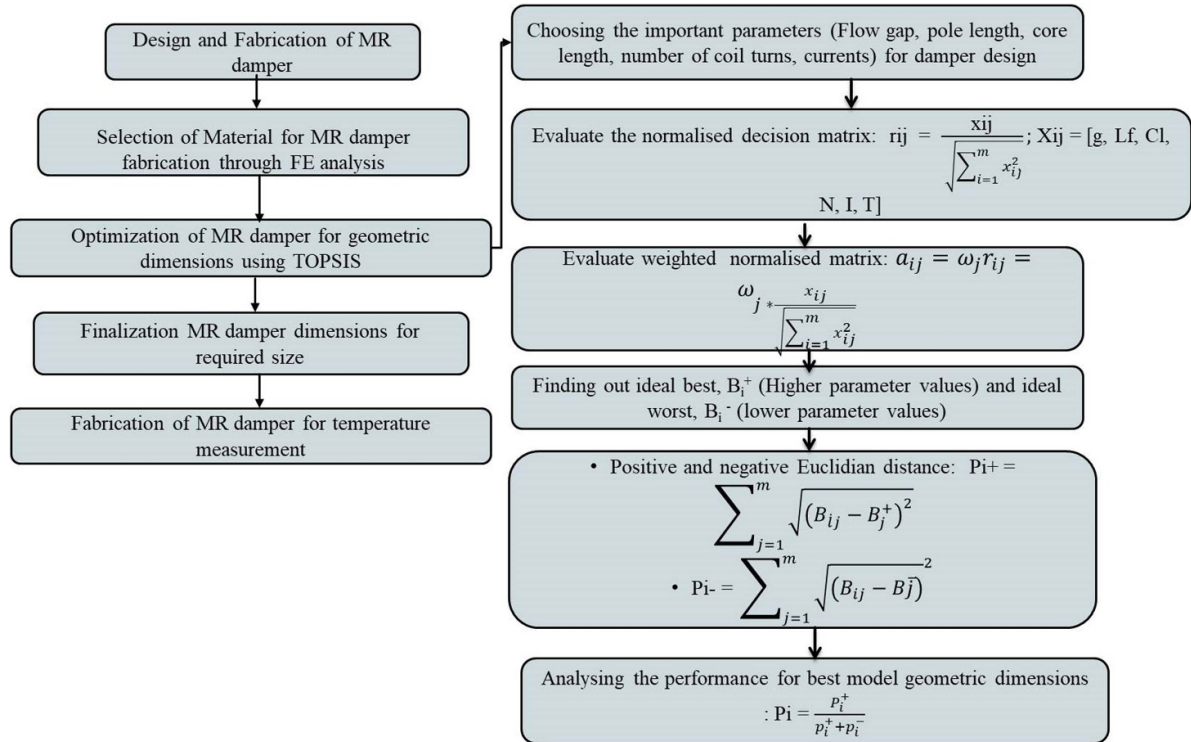


Figure 6. TOPSIS methodology flowchart.

weightage is given to magnetic flux density. They were used for finding the positive and negative Euclidian distance from equations (4) and (5).

$$P_{i+} = \sum_{j=1}^m \sqrt{(B_{ij} - B_j^+)^2} \quad (4)$$

$$P_{i-} = \sum_{j=1}^m \sqrt{(B_{ij} - B_j^-)^2}. \quad (5)$$

The performance score is calculated based on the magnitude of the magnetic flux density produced while calculating ideal best and ideal worst values. Equation (6) gives the formula for performance score calculation.

$$P_i = \frac{P_i^+}{P_i^+ + P_i^-}. \quad (6)$$

The overall goal line of this design of MR damper study is to get geometric dimensions for maximum magnetic flux density in the fluid flow gap and, in turn, to have a better damping force.

4.1. Finite element analysis

The primary objective is to select material for fabrication of the damper. Through step-wise analysis of permeability of the materials in getting optimal damper. According to electromagnetic field theory, the magnetic induction line is almost parallel at the interface between boundaries of the enclosure, fluid,

piston core, and outer cylinder. The relation between magnetic flux and magneto-motive force in the piston core and cylinder can be obtained through Ohm's law which is given below

$$\Phi = NI/R_m \quad (7)$$

where Φ is the magnetic flux, N = number of turns, I am the current, and R_m ($1 \mu\text{A}^{-1}$, μ is the magnetic permeability of the material, and A is the cross-sectional area of the circuit) is the resistance offered by the magnetic circuit. Magnetic flux density (B) is computed from the current flux density (J) of the applied DC, and this current density is further used to evaluate the magnetic field intensity (H), which was developed using Ampere's law and Gauss law of magnetism and are given by

$$\nabla \times H = J + dD/dt \quad (8)$$

$$\nabla \cdot D = \rho$$

Magnetic flux density is given by [51]

$$B = \mu_0 NI/2 \times g \times \mu_r \quad (9)$$

where ρ = free electric charge, $J = I/A$, current density, D = electric flux density, g = fluid flow gap (mm), μ_r = relative permeability of MR fluid, μ_0 = magnetic permeability of free space.

The material properties of the damper have been considered with the exact dimensions of fluid flow gap, pole length, and core length with non-magnetic materials for outer cylinder and piston rod for damper-1 and magnetic materials for same cylinder and piston rod for damper-2.

Table 3. Models used for selection of MR damper dimensions.

Models	Effective length	Core length	Coils	Fluid gap	Magnetic flux density
Mod-1	3	15	300	0.5	0.671
Mod-2	4	18	450	2	0.842
Mod-3	5	21	400	1	0.906
Mod-4	6	24	350	2.5	0.549
Mod-5	7	27	500	1.5	1.01

Table 4. Weightage is given to each design parameter.

Flange length (mm)	Core length (mm)	No. of coil turns	Shear gap (mm)	Magnetic flux density
0.1	0.1	0.1	0.2	0.5

4.2. Geometric dimensions for MR damper fabrication

Design dimensions for the fabrication of the damper are obtained from the TOPSIS method, which can be exclusively employed in many engineering applications where more than one objective is involved (minimising one parameter by maximising another parameter). The principle of operation is based on the user's requirements, which gives closeness to the ideal solution [52]. The advantage of this method is that the user can place the various magnitude of importance on the objectives that one wishes to employ that depends on application and interest. This is done by placing different weights on the objective functions. In this section of the study, multiple parameters that decide the performance of the damper (contrary parameters) are studied based on weightage given to parameters given by the user on beneficial/non-beneficial terms. This method aims to see the importance of each parameter that contributes to the increase in the magnetic flux density in the fluid flow gap. As discussed earlier, the design parameters include effective length, core length, and the number of coils, currents, and fluid flow gap. The five models with different dimensions are selected within the required limits by assigning the weightage to each parameter and obtaining the parameters which give the highest magnetic flux density is selected for fabrication. From the previous literature, study fluid flow gaps play a significant role in obtaining the highest magnetic flux density. Based on this literature, available weights are assigned. The model dimensions and the weights used to obtain the dimensions were given in tables 3 and 4. Taking fluid gap as the non-beneficial criteria and giving more weightage to the magnetic flux density in the fluid flow gap by maintaining the applied current constant at 1.5 A, the performance scores of individual models are given in table 5. The dimensions obtained for fabrication are given in table 6.

4.3. Fabrication of MR damper

After material selection, the fabrication process is carried out on traditional machining processes based on the dimensions obtained from the previous section. To vary the magnetic field electrical cables has to be passed through the hole drilled

Table 5. Performance score of all the models.

Model-1	0.51858
Model-2	0.46935
Model-3	0.73768
Model-4	0.16195
Model-5	0.73016

Table 6. Selected dimensions for fabrication.

Parameters and their final dimensions for fabrication MR damper	
Flange length	5 mm
Shear gap	1 mm
Core length	21 mm
Number of copper turns	400
Maximum operating current	1.5 A

(3 mm) in piston rod and to measure the temperature thermocouple (*K*-type) is passed along with electrical cables until the top of the piston head. A copper coil is wound using the mechanical winding machine, which has a dial for counting the number of turns on the piston core material. Figure 7 shows the complete MR damper arrangement for characterisation along with the thermocouple tip on the piston head.

4.4. Characterisation of MR damper

The complete arrangement to measure the temperature inside the damper is shown in figure 8. The structure consists of a damper testing machine fitted with an MR damper. The *k*-thermocouple is inserted where one side of the bead comes in contact with fluid on top of the piston head. During the continuous operation of the MR damper, the movement of the liquid from the flow gap comes in contact with the thermocouple bead, measuring the temperature of the fluid. Inline by measuring the fluid temperature inside, there were other two thermocouples connected onto the surface of the outer cylinder, T_{S1} -top surface, and T_{S2} bottom surface. Temperature and force-displacement data are acquired simultaneously with

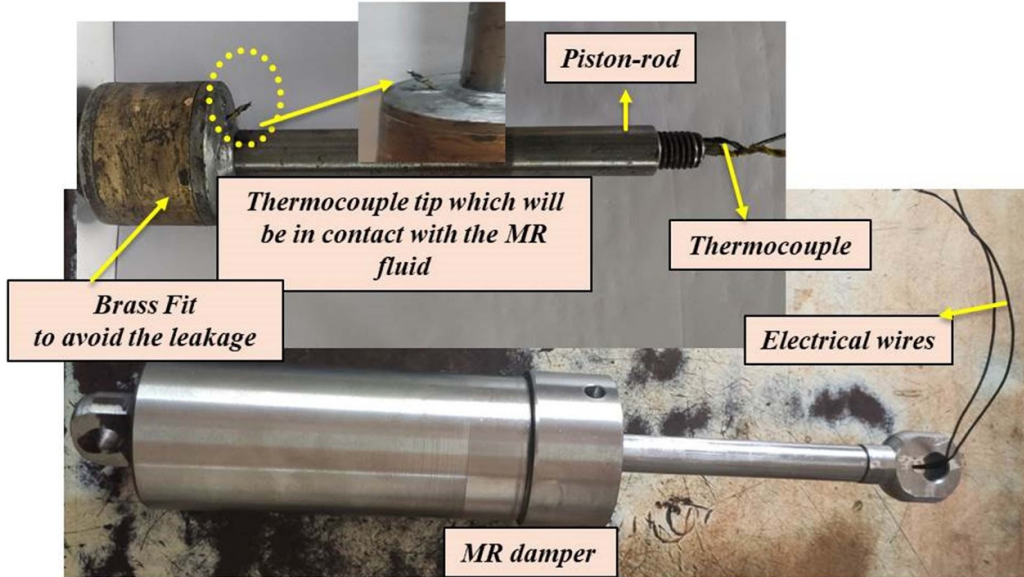


Figure 7. Arrangement to measure the temperature of the MR fluid inside the damper.

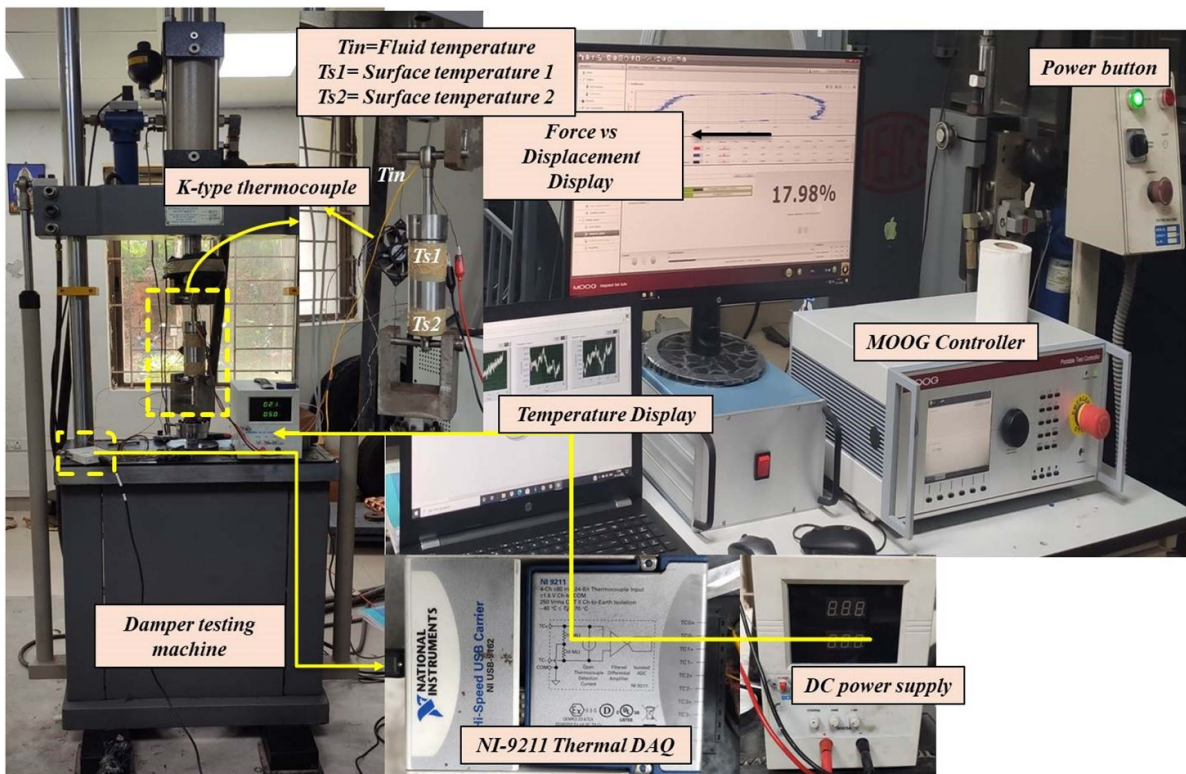


Figure 8. DAQ and controller setting for temperature characterisation.

NI-9211 thermal DAQ and inbuilt data acquisition through the controller of the damper testing machine, respectively. The force data is acquired from the load cell attached at the bottom fixture. The displacement given to the damper is acquired from the displacement transducer attached at the top and the hydraulic actuator. The current is supplied with the help of the dc power supply.

4.5. Theoretical study on heat generation in MR damper

The temperature of the MR fluid plays a significant role in the MR damper's performance and affects the life of the system operating under these fluids. A theoretical model was modelled and validated experimentally to study the model's applicability. Using lumped system analysis proved academic

experimentation results for different damping forces. A control volume is selected within the damper where energy balance in rate form is applied upon solving the relation gives the temperature at any instant [43]. By converting the obtained model to nondimensional terms to get the heat leaving the system and heat generated from the applied current. The important assumptions in order to prove the applicability of the lumped phenomena were variation in yield stress of the MR fluid between atmosphere and the system is not more than 5% and also Biot number should be less than 0.1 [53]. The energy balance is given by

$$Q - W = \frac{dU}{dt} \quad (10)$$

where Q = heat transfer rate, W = the work supplied and $\frac{dU}{dt}$ = internal energy of the system.

The heat is leaving the system through convection is given by the equation below

$$Q = hA_s [T(t) - T_0] \quad (11)$$

where h = convective heat transfer coefficient, A_s = external surface area of the damper, T_0 = ambient temperature, $T(t)$ = temperature at any instant of time.

Work done in this equation (10) is given by two terms one is force-displacement, and another is electricity supplied and is given below

$$W = F(t) \times \frac{dx(t)}{dt} - I^2(t)R \quad (12)$$

where $F(t)$ is the work input to the piston rod, $x(t) = \bar{x} \sin(\omega t)$, I = input current, R = resistance of the wire.

Constitutive law is used to represent the inherent nonlinearity in the MR damper is assumed to be equation (13).

$$F(t) = C \times \left| \frac{dX(t)}{dt} \right|^\alpha \operatorname{sgn} \left(\frac{dX(t)}{dt} \right) \quad (13)$$

where C and α ($0 \leq \alpha \leq 1.5$), are the functions of current and temperature, and they are damping coefficient and fractional exponent, which shows the inherent nonlinearity in the MR damper.

The internal energy within the control volume is given in equation (14).

$$\frac{dU}{dt} = \frac{dT(t)}{dt} \sum m c \hat{p} \quad (14)$$

where $\frac{dT(t)}{dt}$ = rate of temperature change in the system, $\sum m c \hat{p}$ = summation of all the internal energies. Substitution and rearranging of terms give

$$T(t) + \lambda [T(t) - T_0] = \frac{C \bar{x} \cos(\omega t)}{\sum m c \hat{p}} |\bar{x} \omega \cos(\omega t)|^\alpha \times \operatorname{sgn} \left(\frac{dX(t)}{dt} \right) + \eta \quad (15)$$

where $\lambda = \frac{hA_s}{m c \hat{p}}$, $\eta = \frac{I^2 R}{\sum m c \hat{p}}$.

For MR fluid damper 4th order Runge–Kutta method is used to solve the equation (15) for any value of α .

5. Results and discussion

The detailed results of particle analysis, synthesis, sedimentation study, characterisation, design, and characterization of the damper for thermal analysis are discussed in the following section.

5.1. Particle characterisation

The mean particle size of CI particles is $7.42 \mu\text{m}$ when measured with a PSA. The shape of the particle is spherical, which is given by SEM analysis and can be seen from figures 9(a) and (b). Shape and size play an essential role in MR fluids' stability and yield behaviour. As the particle size increases, the sedimentation rate also increases. From figure 9(c), the peaks are obtained at 45.3° , 65.71° , and 82.94° , which correspond to 2θ at 110, 200, and 211 lattice planes which imply that the crystal structure is a body-centered cube.

5.2. Sedimentation stability

The sedimentation results show that, at 30°C , 28% of MR particles have been settled, and it takes nearly 336 h to settle down completely. The fluid temperature is increased from 30°C to 100°C with an increment of 10°C . At each temperature, the time corresponding to sedimentation is noted down. Figure 10(a) shows the details of the sedimentation ratio at individual temperatures. The variation of sedimentation rate at different temperatures was observed for 2% sedimentation, i.e. time is taken for 2% sedimentation at a particular temperature. The results were characterised using an exponential curve shown in figure 10(b).

5.3. Temperature effect on the MR fluid viscosity

For various temperature and magnetic field strengths of MR fluid, shear rate versus viscosity were plotted from varying shear rates. MR fluid viscosity without magnetic field in between temperatures of 25°C – 150°C and with magnetic field in the temperature range of 25°C – 55°C were obtained as shown in figures 11(a)–(d) and 12. The comparative study of in-house fluid viscosity with commercial fluid resembles the same trend at higher temperatures without magnetic field. However, increase in viscosity with magnetic field increase and temperature of MR fluid up to 0.530 T. Above 0.530 T magnetic field, viscosity does not change significantly because of the magnetic saturation of particles. Nevertheless, the decrease in viscosity is exponential with the shear rate. The curve fitting method obtains the relationship between the viscosity and temperature, given by equation (16).

The experimentation found it to decrease exponentially with the increased temperature at various magnetic fields.

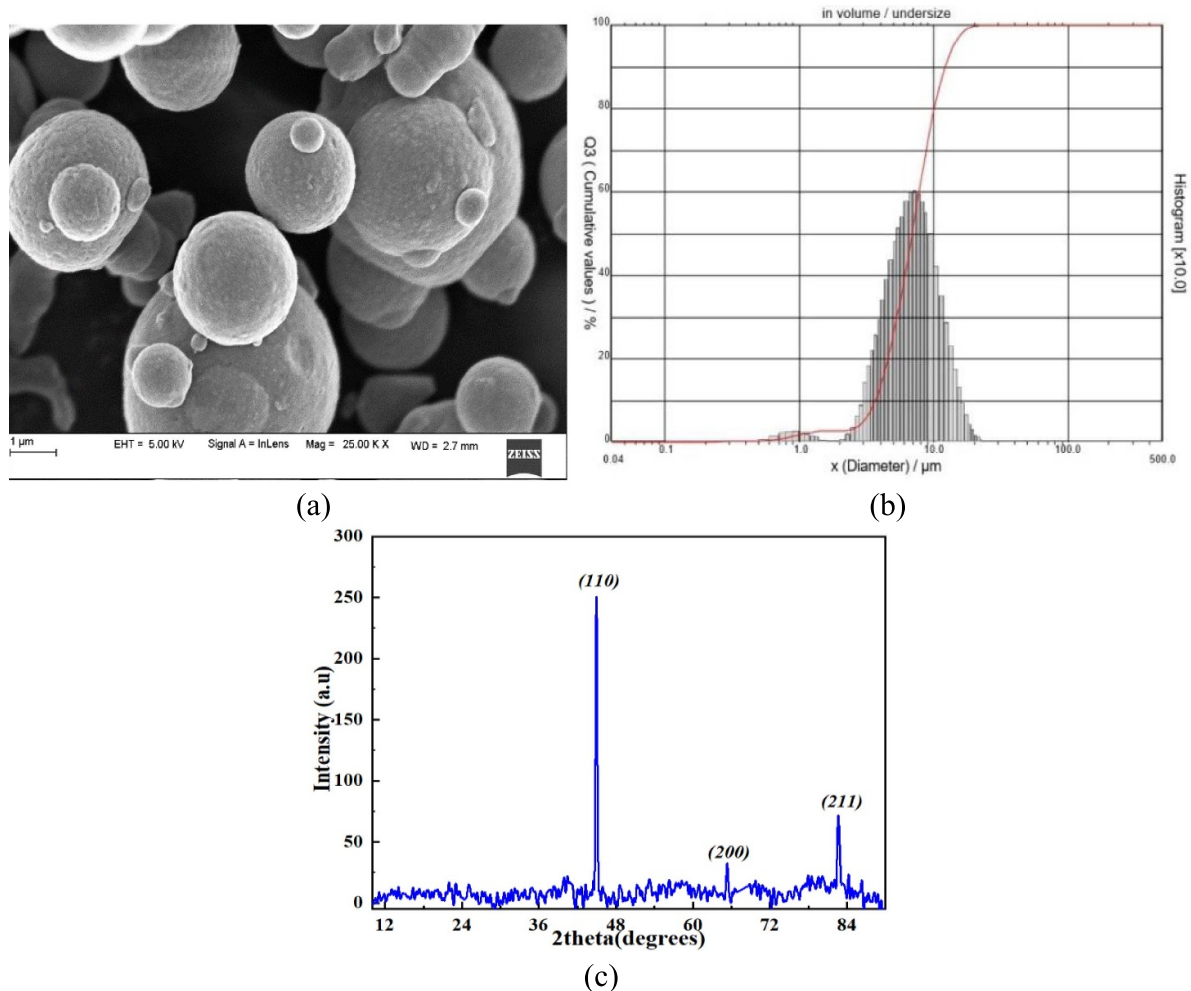


Figure 9. (a) SEM image; (b) PSA of CI particles; (c) XRD of CI particles.

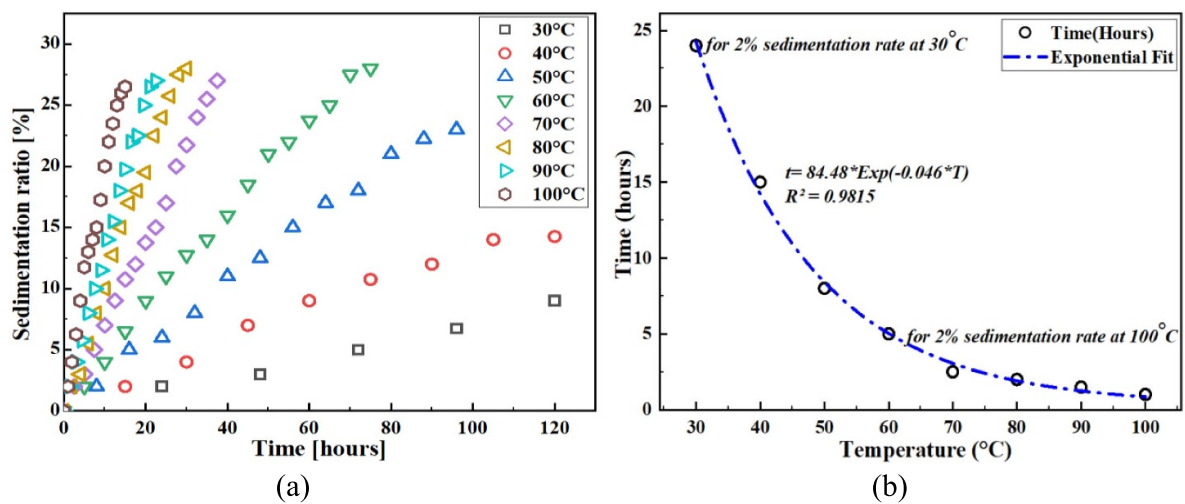
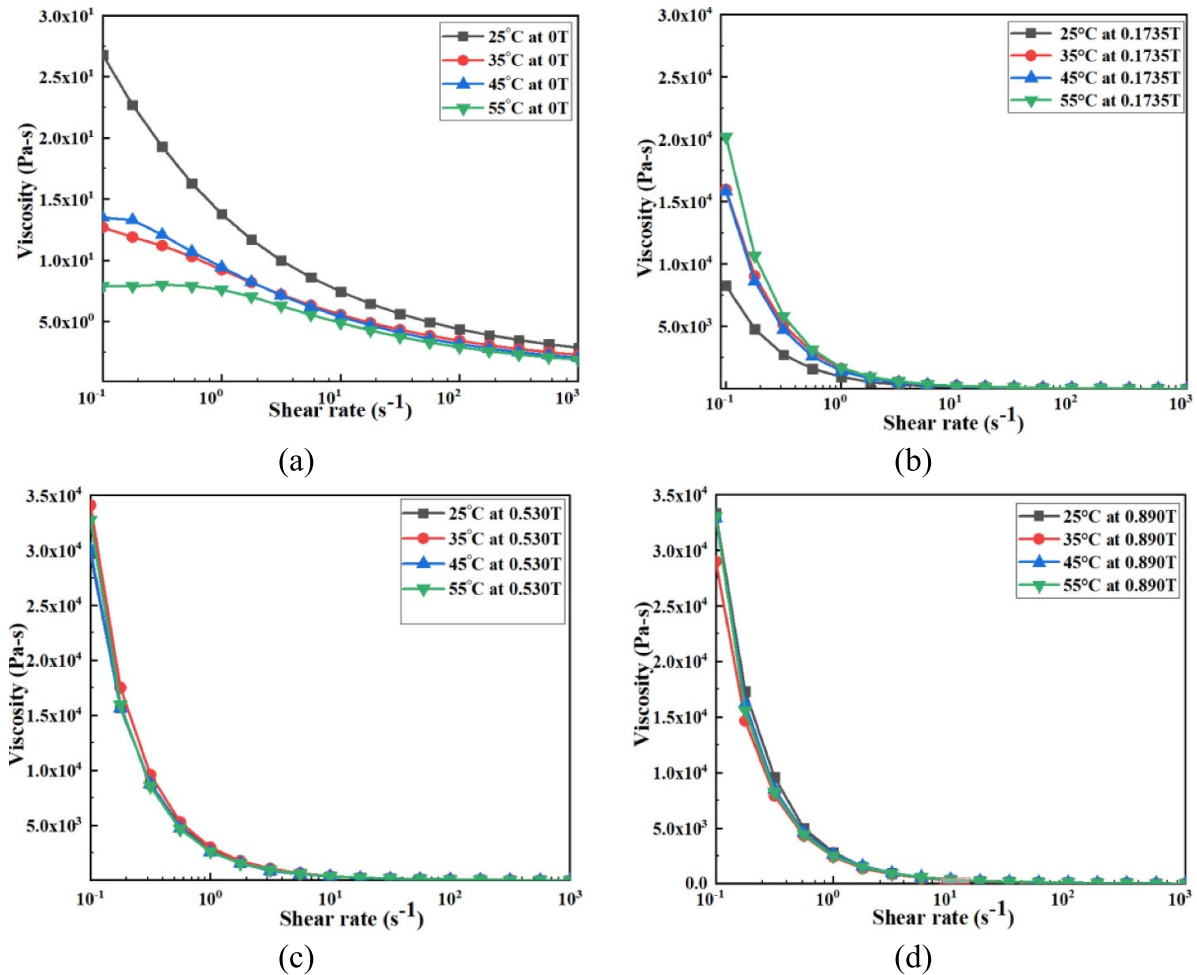


Figure 10. (a) Sedimentation ratio of MR fluid sample at various temperatures; (b) sedimentation rate at individual temperatures.



Figures 11. (a)–(d) Viscosity curves at different magnetic fields.

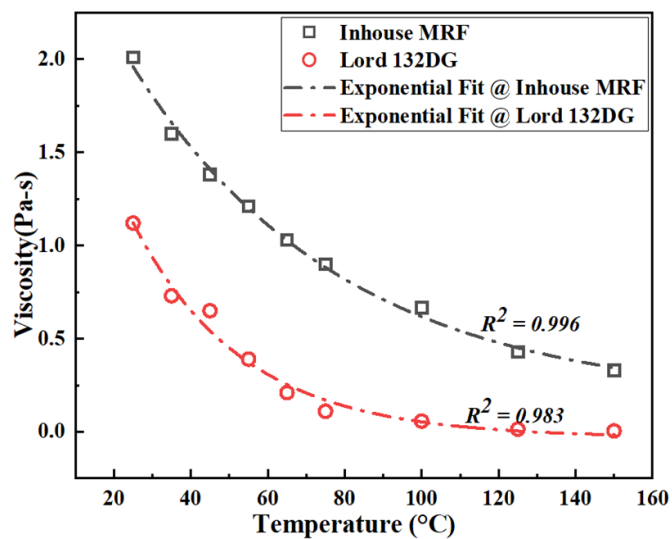


Figure 12. Temperature versus viscosity at zero magnetic field.

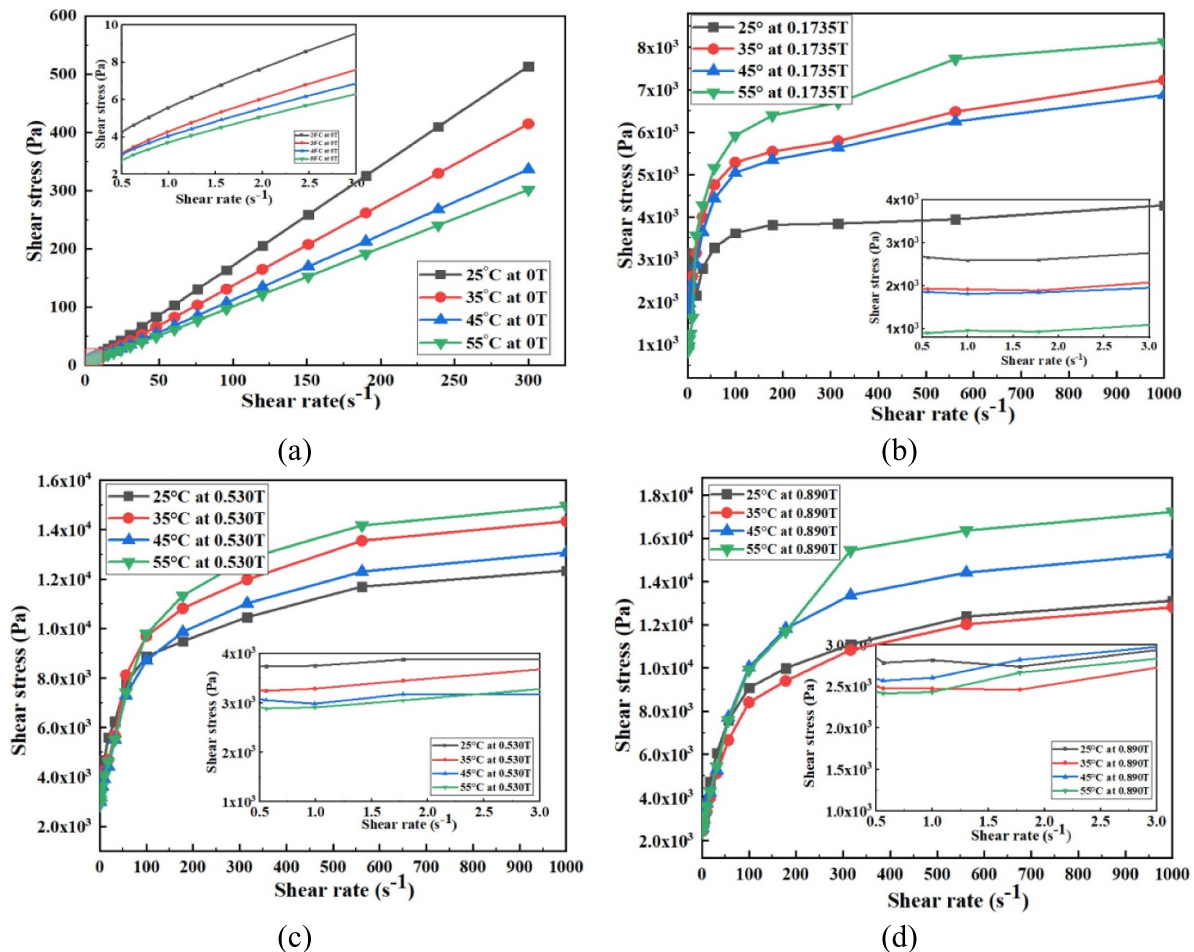


Figure 13. (a)–(d) Shear stress versus shear rate at varying temperatures and magnetic fields.

The equation for the exponential curve is given below

$$\mu = a e^{-bT} \quad (16)$$

where a and b are constants, T = temperatures, μ = viscosity (Pa s).

5.4. Temperature effect on MR fluid yield stress

To describe the flow behaviour of MR fluid, HB model at varying shear rates and magnetic fields is used. The model comprises Newton's law, power-law, and Bingham plastic law and is expressed by equation (17).

$$\tau = \tau_B + K(\dot{\gamma})^n \quad (17)$$

where τ = shear stress (Pa), τ_B = field (H)-dependent yield stress (Pa), $\dot{\gamma}$ = shear rate (s^{-1}), K = consistency index and n = flow behaviour index.

The flow behaviour of MR fluid at various temperatures and magnetic fields is obtained and is shown in figures 13(a)–(d). It is clear that when the external field is applied, the nonlinear HB model fits the flow behaviour. The available literature study shows that MR fluid properties are mainly affected by temperature. At zero magnetic fields, MR fluid has a yield stress of

4.27 and 2.75 Pa at 25 °C and 55 °C temperatures, respectively, and there is a 35.59% decrease in the yield stress. At a magnetic field strength of 0.890 T, the MR fluid has 2760.3 and 2423.1 Pa dynamic yield stress at temperatures 25 °C and 55 °C, respectively. Approximately a 12.21% decrease in the yield stress was detected at 25 °C to 55 °C with a magnetic field. Higher magnetic fields increase the yield stress at constant temperature up to the saturation point. An increase in temperature at a definite magnetic field reduces yield stress.

Generally, microparticles will have high magnetic properties compared to nanoparticles. When the magnetic field increases, the chain formation filling gaps between the microparticles will increase the yield stress. To modify the HB model and include the temperature effect. First, the change in parameters has to be analysed at different temperatures. Tables 7–10 show the model parameters at different temperatures. The analysis shows that temperature affected yield stress, consistency index, and fluid viscosity, which agrees with the research carried out in the previous studies. At lower shear rates, the flow behaviour curve slope is more than that at higher shear rates. The decrease in yield stress is also due to temperature rise and the Brownian motion of nanoparticles. The Brownian movement comes into the picture because of the

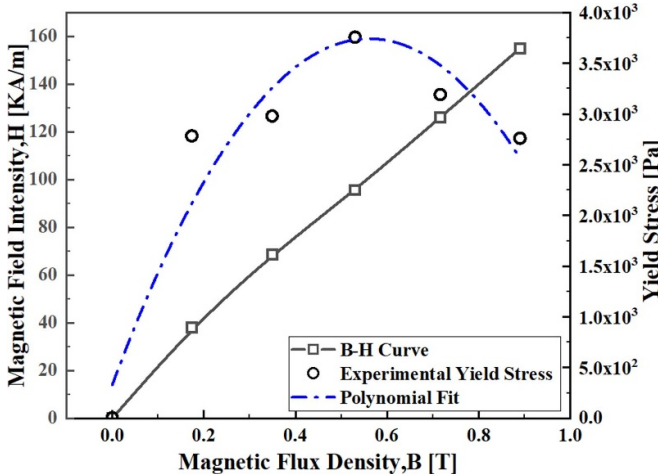


Figure 14. Yield stress variation concerning the external magnetic field at 25 °C.

existence of nanoparticles in smaller quantities that causes a reduction in yield stress [45]. The decrease in yield stress of the MR fluid after a certain magnetic field depicts the fluid's saturation point in magnetic particles and is shown in figure 14.

The B - H curve for equipment shows us that a magnetic field passes through the fluid on the plate. The second-order polynomial equation is fitted over the data obtained and is expressed in equation (18).

$$\tau_B = a_0 (B^2) + a_1 (B) + a_2 \quad (18)$$

where a_0 , a_1 , and a_2 are constants, B = Magnetic flux density [T].

Figure 15 shows the dependency of consistency index K on the applied magnetic field has been fitted with a 2nd order polynomial and given by equation (19).

$$K = -115.6 (B^2) + 943.36 (B) + 93.41. \quad (19)$$

Based on figures 16(b), a curve has been fitted considering the temperature and magnetic field effect; the HB model is incorporated by adding the Arrhenius equation (decaying impact) and is shown by equation (20). The parameters were calculated using the equation mentioned in table 11. This model will be further implemented in CFD simulation work.

$$\tau (T, \gamma) = \tau_B (B) A_1 (T) + K(B) A_2 (T) \dot{\gamma}^n \quad (20)$$

where A_1 and A_2 are the exponential decay functions representing the temperature effect on MR fluid yield stress and viscosity.

$$A = A_0 \text{Exp} (E_a / R.T) \quad (21)$$

where A_0 = pre-exponential parameter, E_a = activation energy, R = universal gas constant = 8.314 J K⁻¹.mol, T = temperature.

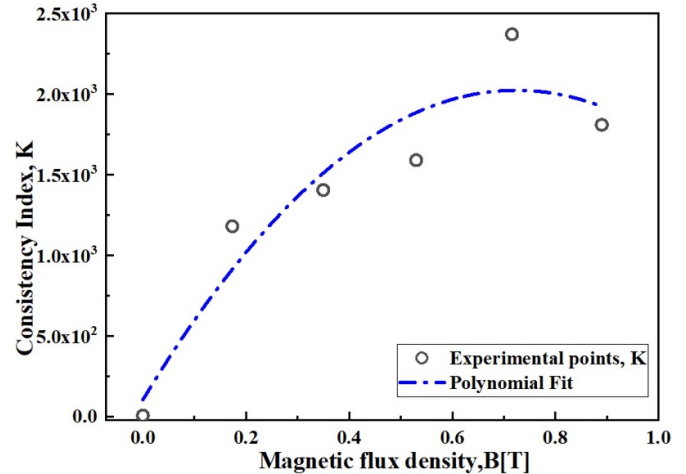


Figure 15. Magnetic field versus consistency index.

6. Design and fabrication of MR damper

Before fabrication, the materials used for fabrication are selected based on the FE analysis, and dimensions were determined from the TOPSIS technique.

6.1. Selection of material for MR damper fabrication

The selection of materials for the fabrication of MR damper is studied through FE analysis of ANSYS workbench and to find out induced magnetic field in the fluid flow gap at different current inputs, which also decides the performance of MR damper. Figure 17 gives the schematic representation of the MR damper. The other vital parameters which enhance the magnetic flux density in the damper are the materials of a piston, cylinder, and design dimensions of the damper. The selected materials for the analysis are shown in table 12.

The results from FE analysis show that the magnetic materials with high permeability give a higher value of magnetic flux density in the flow gap than the non-magnetic materials with less magnetic permeability. Figure 18(a) (damper-1) below shows us the leakage of a large amount of magnetic flux from the damper to the ambient, and figure 18(b) (damper-2) indicates no magnetic flux leakage from the ambient. Figure 19 shows us the magnetic material used for cylinder and piston material for MR damper fabrication.

6.2. Estimation of damping force from FE analysis

Theoretical damping force is calculated based on the magnetic flux density obtained in the gap between the effective length and outer cylinder. FE analysis is employed to obtain the magnetic flux density in the gap and then substituting in equation (2) to find the yield stress of the fluid. The properties such as viscosity, density, specific heat capacity, the permeability of the material are to be added in the equations below. The overall damping force induced in the damper is given by the three forces, i.e. frictional force (F_f), field-dependent yield stress

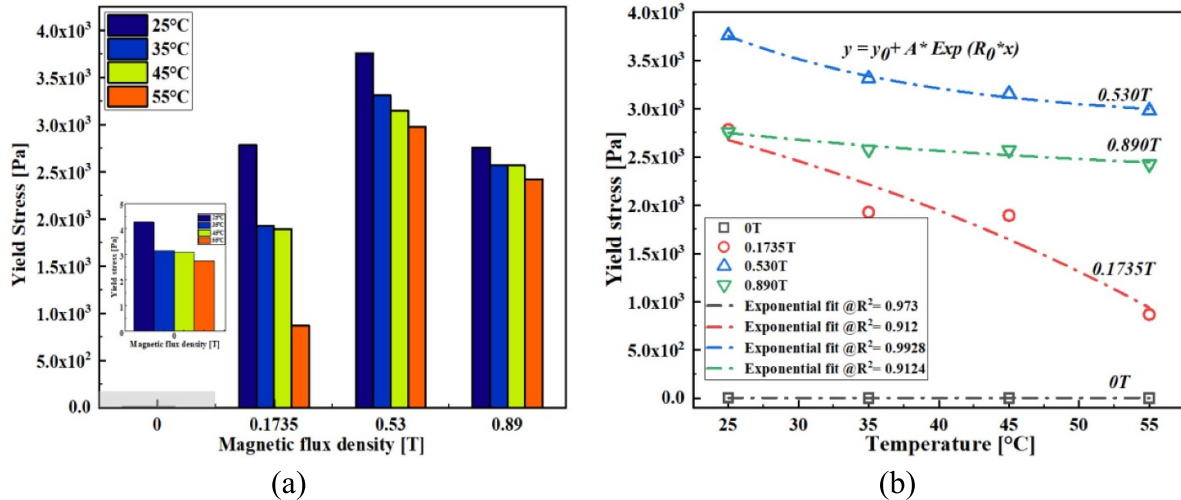


Figure 16. (a), (b) Magnetic field versus yield stress at different temperatures.

Table 7. HB model parameters and yield stress values at different magnetic fields (25 °C temperature).

Magnetic flux density (T)	τ_B (Pa)	K	n	R-square
0	4.27	1.59	1	0.99
0.1735	2784.6	1179.8	0.202	0.94
0.530	3757	1588.64	0.276	0.97
0.890	2760.3	1808.19	0.285	0.960

Table 8. HB model parameters and yield stress values at different magnetic fields (35 °C temperature).

Magnetic flux density (T)	τ_B (Pa)	K	n	R-square
0	3.14	1.24	1	0.99
0.1735	1927.1	1407.49	0.227	0.965
0.530	3313.1	1571.81	0.312	0.96
0.890	2574.32	1491.52	0.31	0.967

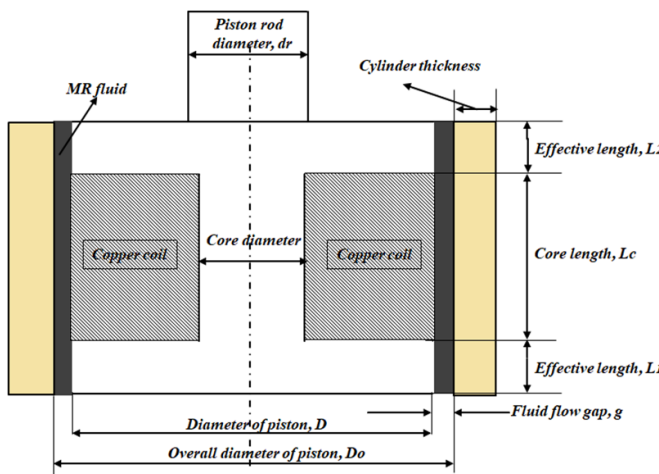


Figure 17. Schematic representation and terminology of the piston.

(F_τ), and viscous force (F_μ), and is shown in equation (22) [54]. In this case, neglecting the friction force, the other two forces are considered for the study.

$$F = F_f + F_\tau + F_\mu \quad (22)$$

$$F_\tau = 2.07 + \left(\frac{12\mu Q}{12\mu Q + 0.4\omega g^2 \tau_B} \right) \frac{\tau_B L A p}{g} \operatorname{sgn}(\dot{u}) \quad (23)$$

$$F_\mu = \left(1 + \frac{\omega g \dot{u}}{2Q} \frac{12\mu Q L A p}{\omega g^3} \right) \quad (24)$$

$$\dot{Q} = \dot{u} A p$$

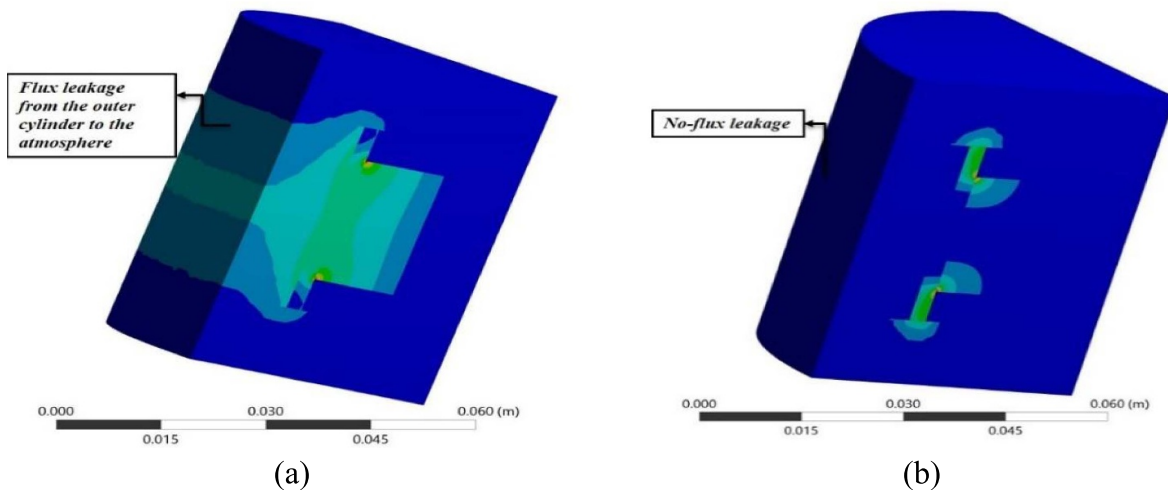
$$\dot{\gamma} = \frac{\text{velocity}}{2 \times \text{flow gap}}$$

Table 11. Parameters of the exponential decay function in various temperature ranges are obtained using equation (20).

Magnetic flux density (T)	Temperatures (°C)	E_a . (τ_B)	E_a (μ)	T_3 (°C)	R^2
0–0.890	25–55	2314.176	340.32	45	0.91

Table 12. Materials used for FE analysis.

Models	Piston core	Piston-rod	Cylinder
Model-1	SA1018	Non-magnetic	Non-magnetic
Model-2	SA1018	SA1018	SA1018

**Figure 18.** Magnetic flux density of (a) damper-1 and (b) damper-2.**Figure 19.** Raw material for MR damper fabrication.

where L = effective length (mm), $L_t = L_1 + L_2$, total effective length (mm), w = average circumference of flow gap (mm), D = diameter of piston (mm), g = gap thickness (mm), μ = apparent viscosity (Pa s), τ = shear stress (Pa), d_o is the diameter of piston rod (mm), Q = volumetric flow rate ($\text{mm}^2 \text{ s}^{-1}$), and u = relative velocity (mm s^{-1}).

6.3. Characterisation of MR damper

This work aims to determine the relationship between the temperature effects on damping behaviour of the MR fluids in damper. The first step in characterization was setting up the MR damper onto the damper testing machine. Before fitting, MR fluid sample is kept in a desiccator vacuum pump to remove the air bubbles trapped in the fluid while stirring in the mechanical stirrer (to avoid air pressure on the piston) and then pouring the calculated fluid volume in the cylinder chamber. Checking the electromagnetic circuit for closeness using a multimeter and simultaneously connecting the thermocouple wires internally and externally to NI-9211 thermal DAQ and this daq to the pc. Figure 20 gives the MR damper characterisation flow chart.

By switching on the damper testing machine, some cycles at random amplitudes, frequencies, and current are operated for checking the smooth operation. After checking with

$$\mu = 0.0006\gamma^{-0.6091}$$

$$w = \pi \left(\frac{g}{2} + \frac{g}{2} + D \right)$$

$$Ap = \frac{\pi (D^2 - d_o^2)}{4}$$

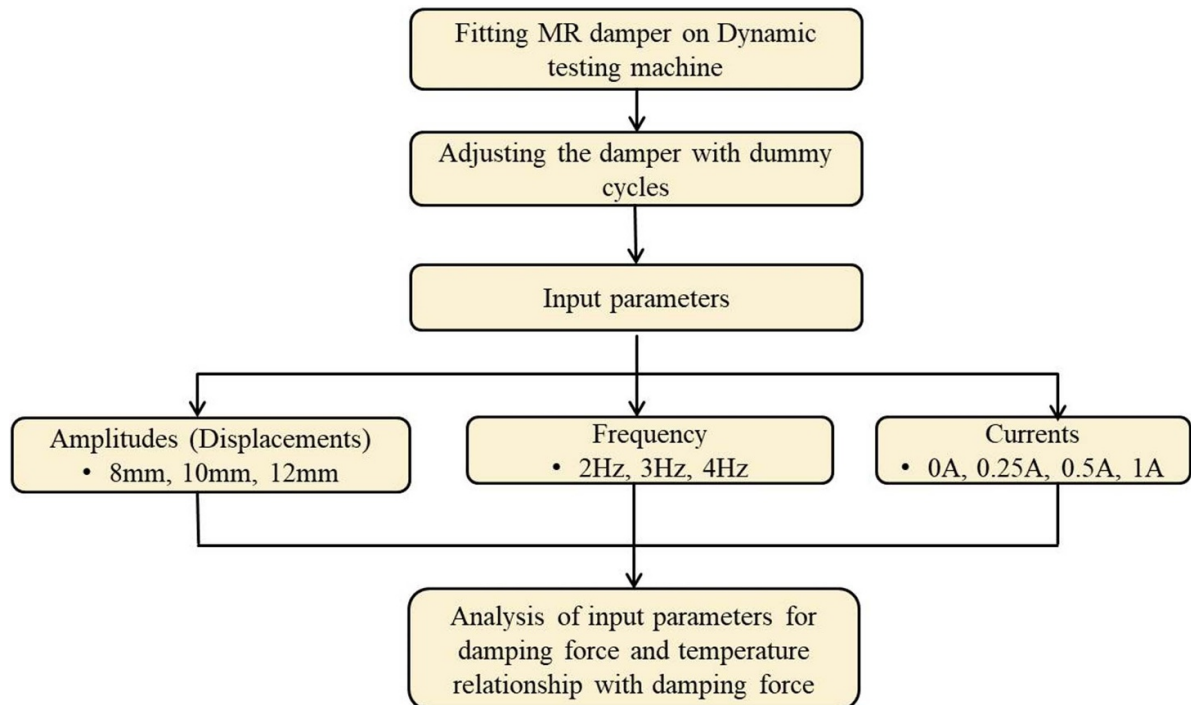


Figure 20. MR damper characterisation flowchart.

random conditions, the input conditions for the test on the damper are set. The amplitudes, frequencies, and currents selected are 8, 10, 12 mm, and 2, 3, 4 Hz, and 0, 0.25, 0.5, and 1 A, respectively. The plots were obtained at a particular amplitude, frequency, and varying currents. This step is repeated for different amplitudes and frequencies. The damping effect of suspension is usually described by force-displacement curves. The area covered by the force-displacement curve shows the damping effect of the damper in that period. Figures 21(a)–(d) shows the force-displacement measurement at 8 mm amplitude, 2, 3, 4 Hz frequencies at 0 and 0.5 A. The test has been carried out for 1000 cycles to see the temperature rise in all the cycles. The distortion in force displacement loop is caused due to the absence of accumulator and presence of bubbles in high viscosity MR fluid which shifts the peak force towards the right side of the force displacement graph. Atmospheric air gets trapped in the process of synthesizing MR fluid forming numerous bubbles in the process of mechanical stirring, due to high viscosity of the carrier fluid trapped air are not escaped easily at low temperatures. Along with accumulator and air bubble effect and inertial and frictional effects also has a minimal impact on force reduction. The characterisation of MR damper in this study is carried out in the absence of the accumulator which is creating average compression load of 36.9% more than the expansion stroke [55, 56]. The air bubble effect also adds to the distortion in force displacement graphs at lower temperatures as the damper operating time increased the temperature of the fluid increases which reduces the viscosity of the fluid making the air escape from the MR fluid decreasing the distortion

in force–displacement graph. The peak force shift towards the left of the force–displacement curve as shown in figure 24(a) [57]. The plots shown below are for the 100th cycle and 1000th cycle to see the increase in temperature and decrease in the damping force at a single stretch for different currents [58]. For instance, in figures 21(a)–(d), 22(a)–(d), and 23(a)–(d) for 8 mm amplitude 2 Hz frequency, there is a decrease of 30 N force and 40.85 °C temperature at 0 A and 60.5 N force decrease and 43.5 °C temperature rise at 0.5 A current. At 10 mm amplitude 2 Hz frequency, there is a decrease in 153 and 340 N decrease in force and 45.9 °C and 48.5 °C temperature increase at 0 and 0.5 A currents, respectively.

For the 12 mm amplitude 2 Hz frequency, the force decrease was 200 and 473 N, and the temperature increase was 42.65 °C and 53.57 °C at 0 and 0.5 A currents, respectively. Taking another instance, at 8 mm amplitude and 3 Hz frequency, there is a forced decrease of 375 and 160 N, and the temperature increase is from 36.2 °C to 46.1 °C at 0 and 0.5 A currents, respectively. At 10 mm amplitude and 3 Hz frequency, there is a 470 and 440 N decrease in force and temperature increase from 54.9 °C to 56.76 °C at 0 and 0.5 A currents, respectively. At 12 mm amplitude and 3 Hz frequency, there is a decrease of 797 and 400 N force and temperature rise are from 57.28 °C to 65.76 °C at 0 and 0.5 A, respectively. At 4 Hz frequency and 8, 10 and 12 mm amplitude, there is a decrease of 780 and 477 N, 680 and 720 N, 868.4 and 1070 N force and 53.5 °C to 53 °C, 63.2 °C to 65.9 °C, 74.2 °C to 79.36 °C temperature increase at 0 and 0.5 A currents respectively. The critical observation is that, as the

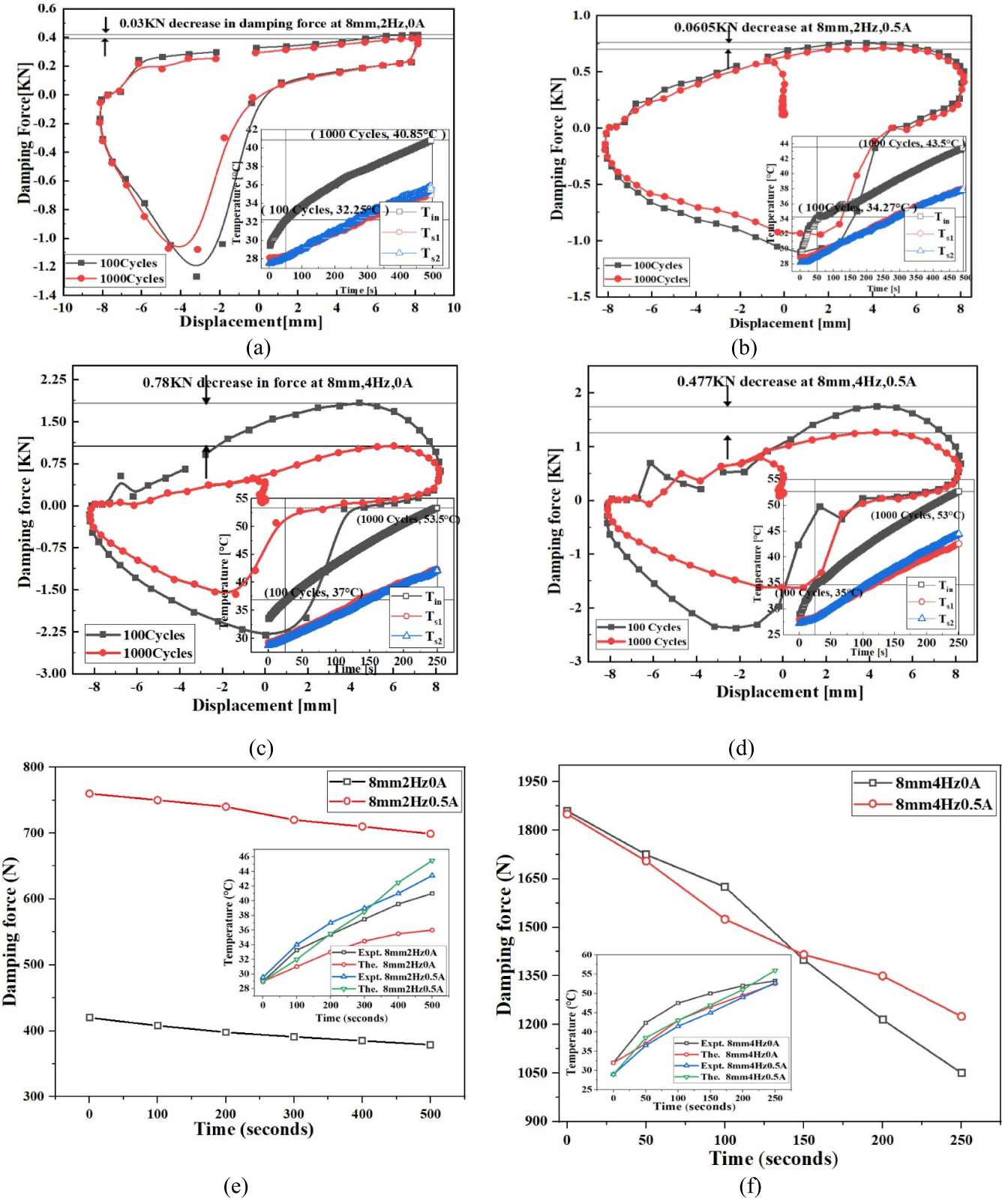


Figure 21. (a)–(f) Peak force reduction and temperature rise at 8 mm amplitude, 2, 4 Hz frequency, at 0 and 0.5 A.

amplitude of vibration increases, the damping force at a particular frequency decreases, causing a temperature increase. And at a specific amplitude and increase in frequency, there is an also enhancement in the damping force decrease and rise

in temperature. The average temperature difference between off state and on state is approximately 8 °C which indicates the rise in temperature with application of current. The amplitude is having a significant impact on temperature rise by

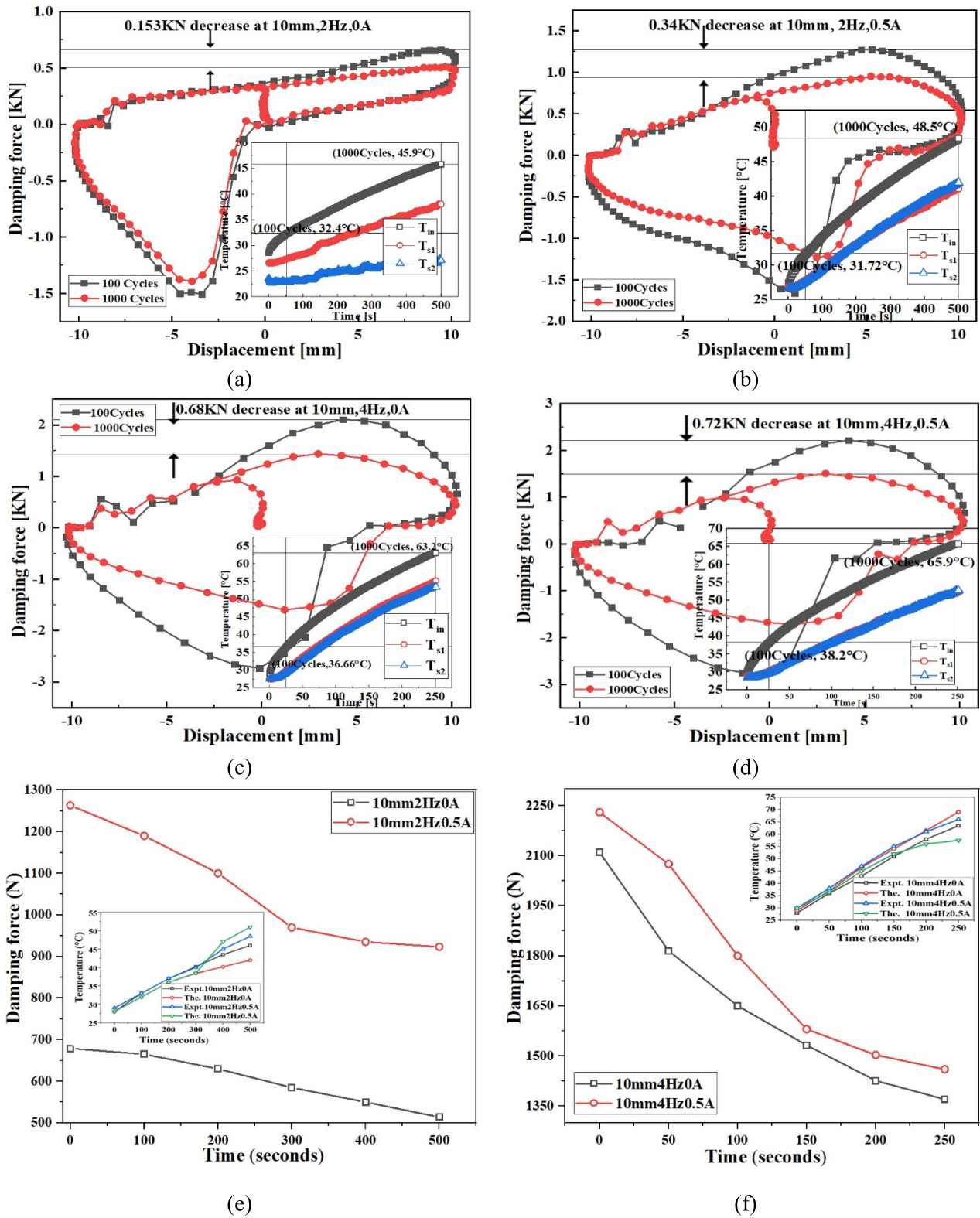


Figure 22. (a)–(f) Peak force reduction and temperature rise at 10 mm amplitude, 2, 4 Hz frequency, at 0 and 0.5 A.

three times more than that of the frequency. Figures 21(e)–(f), 22(e)–(f), 23(e)–(f) and 24(b) shows the peak force decrease with increase in temperature along with theoretical model results with experimental temperature values.

This section also deals with the prediction of temperature inside a damper with theoretical model mentioned in section 4.5 and compared with the experimental values from obtained from the thermocouple which is in direct contact with

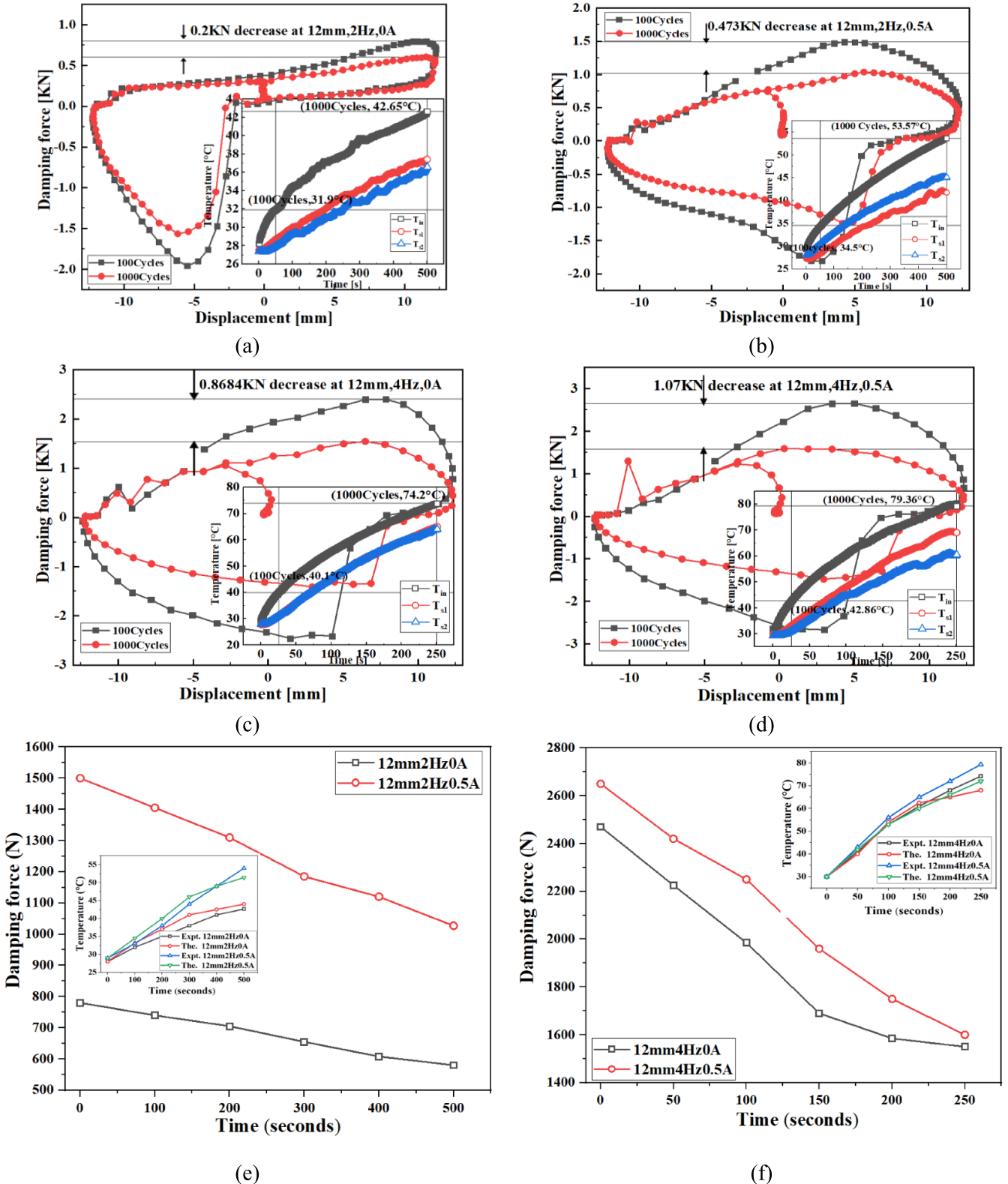


Figure 23. (a)–(f) Peak force reduction and temperature rise at 12 mm amplitude, 2, 4 Hz frequency, at 0 and 0.5 A.

the MR fluid in operation. The known temperature at different time periods and noting the corresponding peak force values, the theoretical temperatures was evaluated. The fluid temperature obtained as a function of time from thermocouple inside

the damper is taken for theoretical comparison. From the previous studies it was shown that varying convective heat transfer coefficient between 28 and 35 $\text{W m}^{-2} \text{K}^{-1}$ has negligible impact on temperature difference for the dampers [53]. For

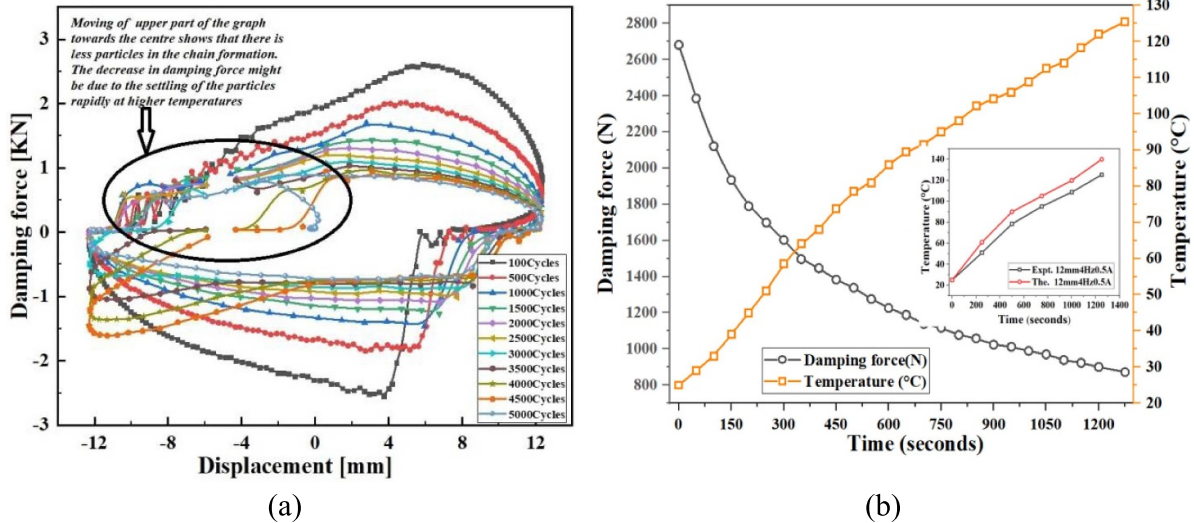


Figure 24. (a), (b) Temperature rise and damping force reduction with time along with theoretical model comparison.

Table 13. Parameter values for theoretical model analysis.

Properties	Values
Heat transfer coefficient, h ($\text{W m}^{-2} \text{K}^{-1}$)	28
Surface area of the damper, A_s (m^2)	0.0336
Total heat capacity of system, $\sum_n mc_p$ (J K^{-1})	1905
Resistance of the electromagnet, Ohms (Ω)	22.4
T_{amb} ($^{\circ}\text{C}$)	25–32

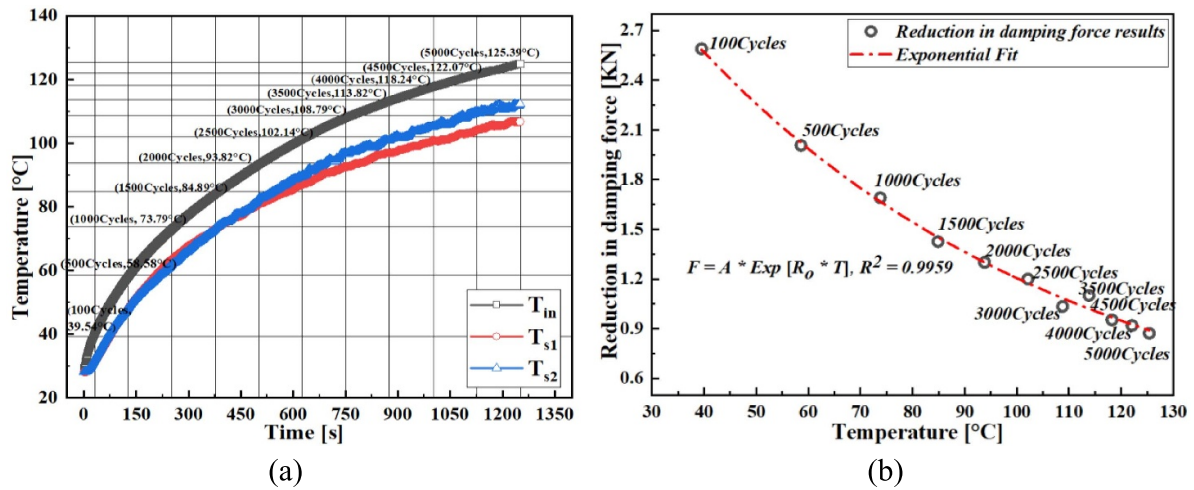


Figure 25. (a), (b) Damping force as a function of temperature.

In the theoretical model analysis in this study, the parameter values were taken is shown in table 13 and the Biot number is 0.007 which is less than 0.1 and satisfies the lumped parameter applicability. Theoretical model also gives the similar observation of increase in temperature and decrease in force as that of the experimental results for amplitude, frequency, and currents with average error of 7.92% and 10.24% at 0 and 0.5 A currents respectively.

It is visible from figures 24(a) and (b), there is a decrease in the area of the force–displacement diagram indicating the

rapid sedimentation of particles with formed chain breakages and energy dissipation into the fluid, making the fluid temperature rise. The relationship between damping force and temperature is obtained by running the damper at 12 mm amplitude 4 Hz frequency, 0.5 A current, and 5000 cycles [59, 60]. One more observation is that there is an increase in the damping force upon increasing the current up to a certain threshold point beyond which there is no increase in the force, which indicates the saturation point of the fluid. The above discussion on amplitude, frequency, currents, and temperature relation

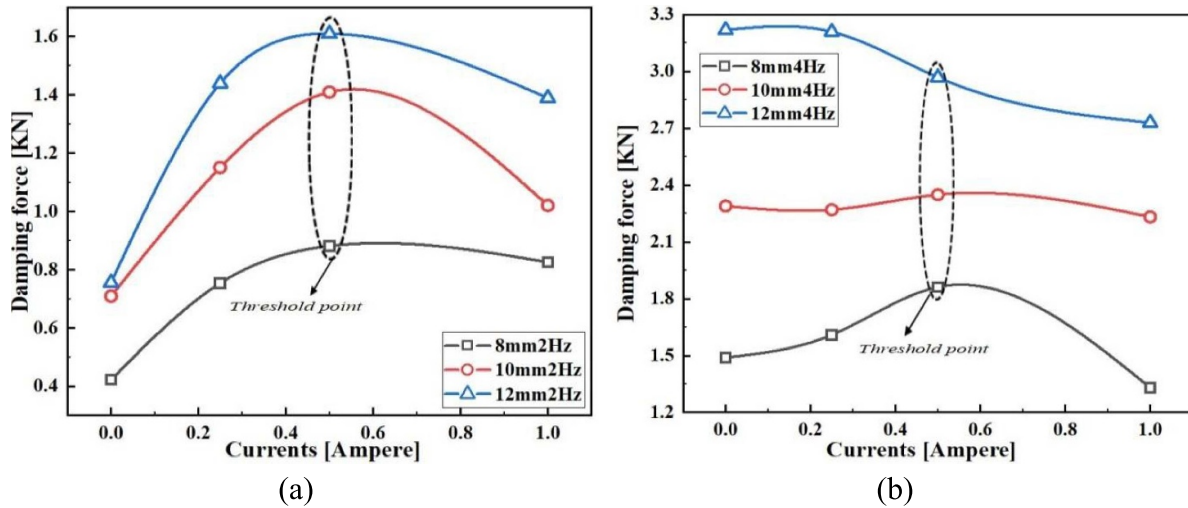


Figure 26. (a), (b) Variation in damping force at different currents.

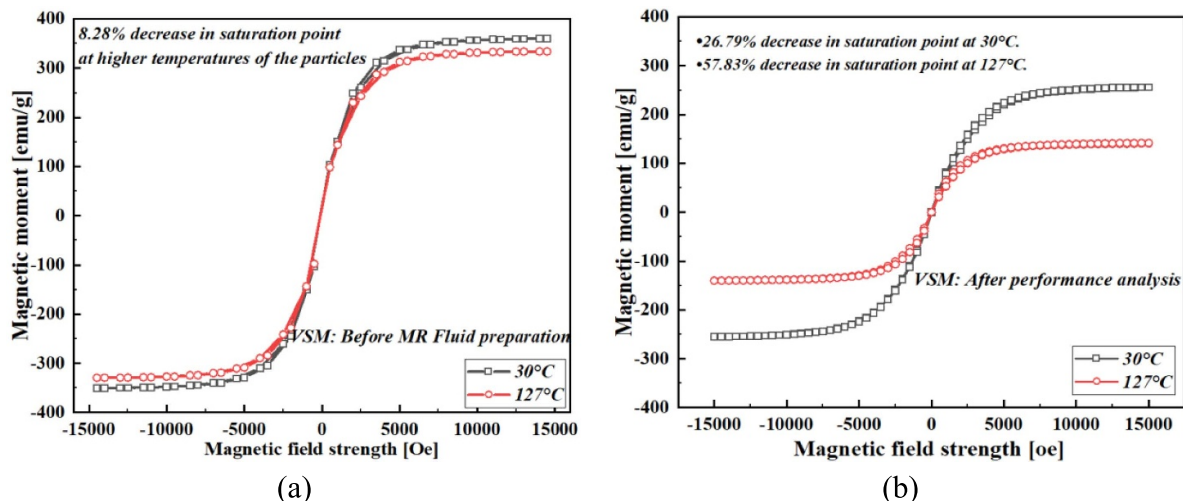


Figure 27. (a) Magnetic saturation before synthesis of MR fluid; (b) magnetic saturation after characterisation of MR damper.

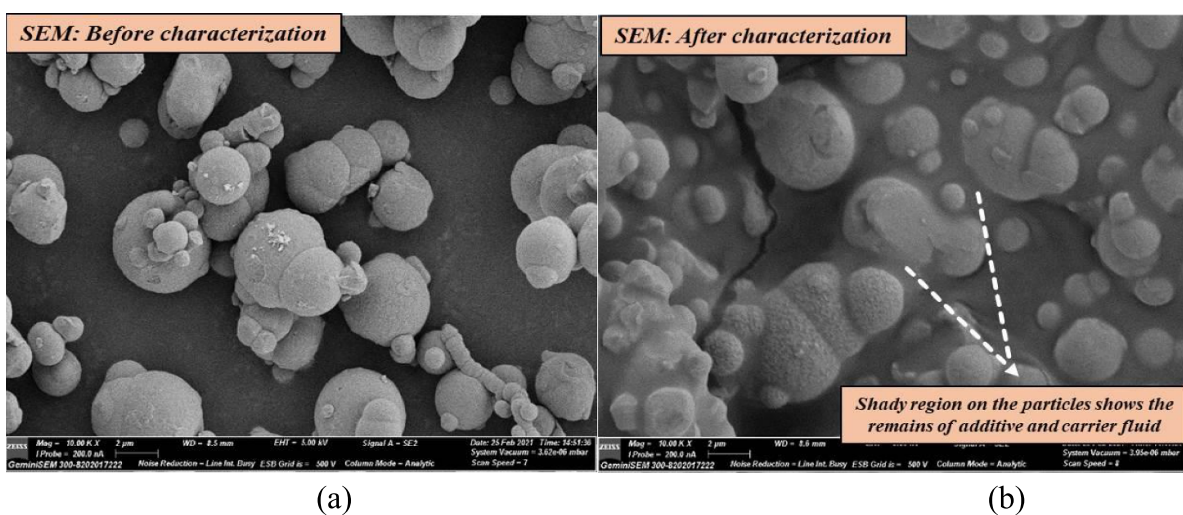


Figure 28. (a). SEM image before synthesis of MR fluid; (b) after characterisation in MR damper.

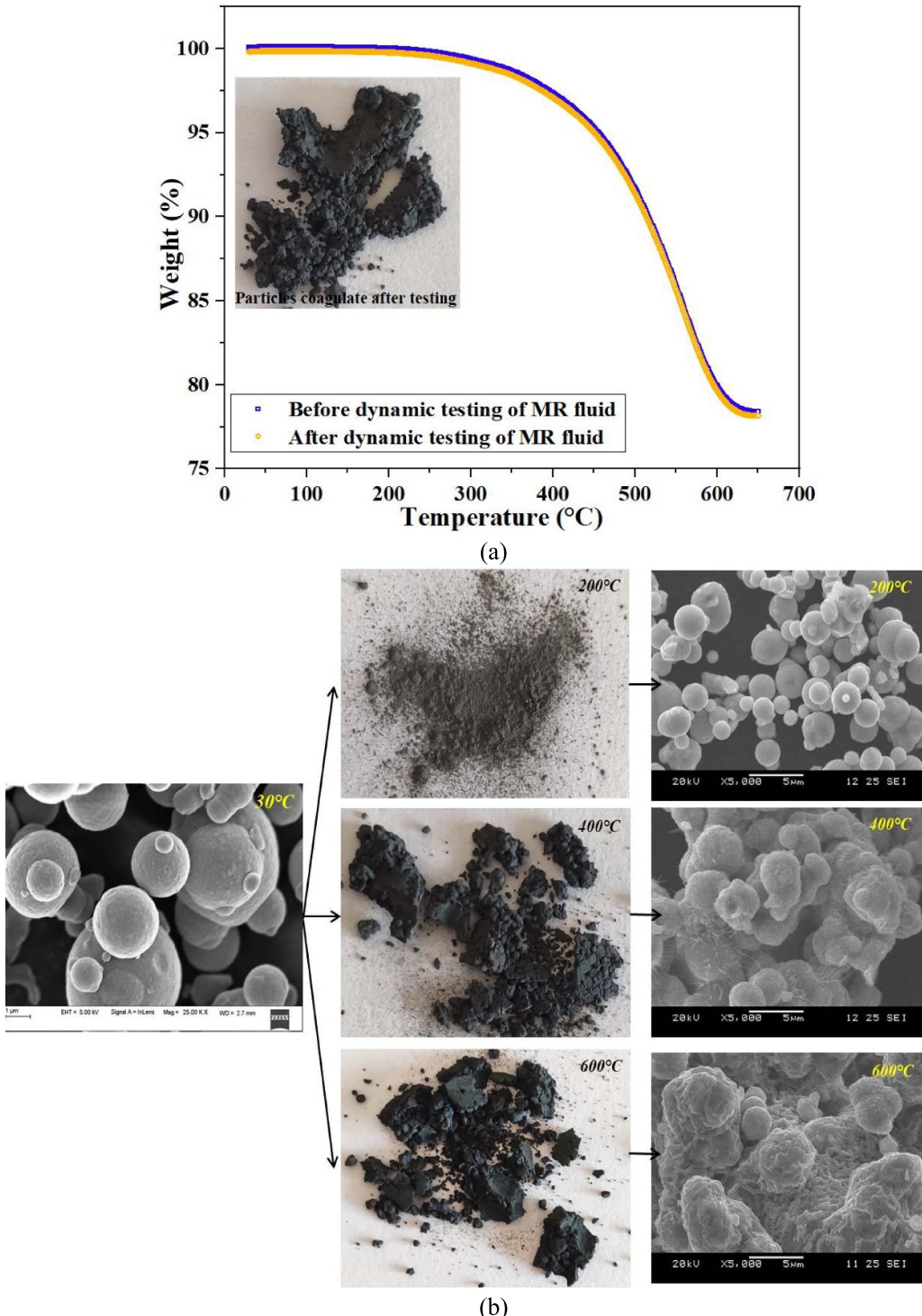


Figure 29. (a) TGA of MR fluid (b) SEM images of heat-treated CI particles.

with damping force and decrease in temperature with insulation on the electromagnet is given in figures 25(a), (b) and figures 26(a), (b), respectively [53, 61].

6.4. Particle analysis after characterisation

After dynamic testing of MR fluid in the MR damper, the particle analysis is fundamental to see the effect of parameters

on particle shape and saturation point of the particles. After operating the damper for approximately about 85 000 cycles which include all test runs and dummy runs at different amplitudes, frequencies, currents, and temperatures, the MR fluid is taken out and cleaned for its carrier fluid and additive using filter paper and acetone and air-dried in the atmosphere for approximately 30 d. The particles sample was tested for particle shape on SEM and saturation magnetisation on the

vibration sample magnetometer. Figures 27(a) and (b) shows the saturation magnetization of the particles at room and higher temperatures before the preparation of the MR fluid and after testing the MR fluid in the damper. The results indicate that at room temperature (30°C), the saturation point is 360 emu g^{-1} , and at higher temperature (127°C), the saturation point reduces to 331 emu g^{-1} , indicating the effect on the performance of the MR fluid. But when it comes to VSM testing after characterisation, at 30°C , the saturation point is 270 emu g^{-1} , and 127°C the saturation point is 145 emu g^{-1} . The reduction in saturation magnetisation is because of the remains of the additive and carrier fluid, which acts as a coating on particles. The change in particle microstructure cannot be considered because of the particle melting point.

Figure 28(a) gives the particle shape before the preparation of MR fluid. Figure 28(b) shows the remains of additive and carrier fluid on the particles compared to particles before fluid preparation. SEM analysis shows no significant change in the shape of the particle after the characterisation. Thermal stability of the MR fluid is carried out on TGA to study the carrier fluid's decrease in weight (%) before and after dynamic characterisation of the MR fluid in the MR damper. Figure 29(a) shows the TGA analysis of MR fluid before and after dynamic testing in the damper. The temperature at which the start of degradation of the MR fluid is 323.3°C for before characterisation and 322.6°C for after characterisation of the fluid, indicating the decrease in stability of the carrier fluid negligible. The carrier's weight reduction is 0.249%, implicating that the silicone base MR fluid retains stability after these amount of cycles. The prolonged operation of the MR fluid makes the fluid temperature more, reducing the fluid's stability. After complete destabilisation of the carrier fluid, the heat is transferred to the particles, making the particle change the shape. To imitate the heating effect, CI particles are heat-treated at 200°C , 400°C , and 600°C in a furnace (with 3%–4% error) for about 15 mins after the furnace reaches steady-state temperature. The samples are tested for SEM images to see the distortion at different temperatures. The images show that, at 200°C there is no change in the morphology but at 400°C particle starts to fuse and at 600°C , the particles start to melt, which is shown in figure 29(b).

7. Conclusions

In this paper, CI-based MR fluids were synthesized in-house and studied for sedimentation with temperature, characterization with nonlinear HB model fit, and temperature effect on fluid performance was captured through thermocouple in MR damper characterized at different loading parameters. The conclusions are as follows

- CI particles of spherical shape were used to prepare MR fluids, and the stability and shear behaviour were studied under different magnetic fields and temperatures. From the sedimentation measurements, the sedimentation rate was found to be reducing exponentially with the rise in temperature of the MR fluid. The study concludes that devices such as

dampers, brakes, or clutches, while in operation, the sedimentation rate is accelerated by the temperature of the fluid. The current study results can be utilized to determine the resting time between two subsequent operations of devices to avoid the temperature accelerated sedimentation.

- In the present experimental investigation, it is observed that the viscosity of MR fluid decreases exponentially as the temperature increases and increases significantly with external applied magnetic field strength. Thus, MR fluid viscosity decreases exponentially with temperature and magnetic field.
- The HB model can capture the nonlinear behavior of in-house MR fluid. However, as the yield stress is affected by temperature and magnetic field, the HB model has been modified to incorporate yield stress as a magnetic field, shear rate, and temperature using the measured data.
- The MR damper's characterization reveals the system's temperature is significantly increased in the decreasing order of amplitude, frequency, and applied magnetic field, i.e. more energy is dissipated into the fluid in amplitude than frequency and magnetic field. The theoretical model predicts a similar temperature rise as the experimental results with an error band of 7.92% and 10.24% at 0 and 0.5 A currents at all the amplitude and frequencies. The reduction in damping force as temperature increases is an exponential drop with $R^2 = 0.9989$. Along with fluid temperature, the magnetic saturation threshold point of the MR fluid decides the upper limit of the damping force.
- The saturation point of magnetization before synthesis of MR fluids reveals an 8.28% decrease at higher temperatures than atmosphere temperature. Finally, the particle analysis on VSM showed a decrease in saturation magnetization by 30% at 127°C temperatures. From the SEM image, it is clear that there is no change in particle shape after operating the MR fluid at different amplitude, frequency, current, and temperature ranges. Further, MR fluid weight reduction is approximately 0.25% through TGA after dynamic testing of the MR fluid, which decides the life of MR fluid which is negligible in this range of cycles. Lower input parameters of amplitude, frequency, and current temperature increase was approximately two times less than higher input parameters for the same amount of operating time. Suppose the operating time of the damper is increased at higher input parameters, temperature increases significantly nearing the destabilization point, which can be evaluated from gravimetric analysis of the MR fluid. Based on the working amplitude, frequency, and currents of the MR system, the safety factor can be set for MR damper operating temperature using TGA results. The heat treatment study of CI particles showed that destabilization of the damper is possible if the system operates at higher temperatures for a prolonged time.

Data availability statement

All data that support the findings of this study are included within the article (and any supplementary files).

Funding statement

This work is supported by the Ministry of Human Resource Development and Ministry of Road Transport and Highways, Government of India, supporting this research through IMPRINT Project No. IMPRINT/2016/7330 titled ‘Development of Cost-Effective Magnetorheological (MR) Fluid Damper in Two wheelers and Four Wheelers Automobile to Improve Ride Comfort and Stability.’

Conflict of interest

The authors declare no competing financial interest.

Ethics statement

The authors declare that this work has not been published elsewhere.

ORCID iDs

Hemantha Kumar  <https://orcid.org/0000-0003-1372-3382>
M Arun  <https://orcid.org/0000-0002-0442-7891>

References

- [1] Sarkar C and Hirani H 2013 Synthesis and characterization of antifriction magnetorheological fluids for brake *Def. Sci. J.* **63** 408–12
- [2] Sarkar C and Hirani H 2015 Effect of particle size on shear stress of magnetorheological fluids *Smart Sci.* **3** 65–73
- [3] Liu Y D, Lee J, Choi S B and Choi H J 2013 Silica-coated carbonyl iron microsphere based magnetorheological fluid and its damping force characteristics *Smart Mater. Struct.* **22** 065022
- [4] Zuzhi T, Fei C, Xiangfan W and Jian W 2016 A novel preparation process for magnetorheological fluid with high sedimentation stability *Mater. Manuf. Process.* **31** 2030–6
- [5] Ashtiani M, Hashemabadi S H and Ghaffari A 2015 A review on the magnetorheological fluid preparation and stabilization *J. Magn. Magn. Mater.* **374** 711–5
- [6] Aruna M N, Rahman M R, Joladarashi S and Kumar H 2019 Influence of additives on the synthesis of carbonyl iron suspension on rheological and sedimentation properties of magnetorheological (MR) fluids *Mater. Res. Express* **6** 086105
- [7] Fang F F, Choi H J and Jhon M S 2009 Magnetorheology of soft magnetic carbonyl iron suspension with single-walled carbon nanotube additive and its yield stress scaling function *Colloids Surf. A* **351** 46–51
- [8] BOMBARD A J F, Knobel M and Alcântara M R 2007 Phosphate coating on the surface of carbonyl iron powder and its effect in magnetorheological suspensions *Int. J. Mod. Phys. B* **21** 4858–67
- [9] Lim S T, Cho M S, Jang I B and Choi H J 2004 Magnetorheological characterization of carbonyl iron based suspension stabilized by fumed silica *J. Magn. Magn. Mater.* **282** 170–3
- [10] Viota J L, González-Caballero F, Durán J D G and Delgado A V 2007 Study of the colloidal stability of concentrated bimodal magnetic fluids *J. Colloid Interface Sci.* **309** 135–9
- [11] Anupama A V, Kumaran V and Sahoo B 2018 Magneto-mechanical response of additive-free Fe-based magnetorheological fluids: role of particle shape and magnetic properties *Mater. Res. Express* **5** 085703
- [12] Jiang W, Zhang Y, Xuan S, Guo C and Gong X 2011 Dimorphic magnetorheological fluid with improved rheological properties *J. Magn. Magn. Mater.* **323** 3246–50
- [13] Morillas J R, Bombard A J F and De Vicente J 2018 Enhancing magnetorheological effect using bimodal suspensions in the single-multidomain limit *Smart Mater. Struct.* **27** 07LT01
- [14] Kwon S H, Jung H S, Choi H J, Strecker Z and Roupec J 2018 Effect of octahedral typed iron oxide particles on magnetorheological behavior of carbonyl iron dispersion *Colloids Surf. A* **555** 685–90
- [15] Shah K, Phu D X, Seong M S, Upadhyay R V and Choi S B 2014 A low sedimentation magnetorheological fluid based on plate-like iron particles, and verification using a damper test *Smart Mater. Struct.* **23** 027001
- [16] Choi H Y, Choi J Y, Park H H, Kim T H, Choi H J and Lee C S 2021 Effect of reduced graphene oxide and MnFe₂O₄ nanoparticles on carbonyl iron for magnetorheological fluids *J. Ind. Eng. Chem.* **98** 140–7
- [17] Wang H, Li Y, Zhang G and Wang J 2019 Effect of temperature on rheological properties of lithium-based magnetorheological grease *Smart Mater. Struct.* **28** 035002
- [18] Rabbani Y, Ashtiani M and Hashemabadi S H 2015 An experimental study on the effects of temperature and magnetic field strength on the magnetorheological fluid stability and MR effect *Soft Matter* **11** 4453–60
- [19] Wong P L, Bullough W A, Feng C and Lingard S 2001 Tribological performance of a magnetorheological suspension *Wear* **247** 33–40
- [20] Zhang X Z, Gong X L, Zhang P Q and Wang Q M 2004 Study on the mechanism of the squeeze-strengthen effect in magnetorheological fluids *J. Appl. Phys.* **96** 2359–64
- [21] Jha S and Jain V K 2009 Rheological characterization of magnetorheological polishing fluid for MRAFF *Int. J. Adv. Manuf. Technol.* **42** 656–68
- [22] Song K H, Park B J and Choi H J 2009 Effect of magnetic nanoparticle additive on characteristics of magnetorheological fluid *IEEE Trans. Magn.* **45** 4045–8
- [23] Hato M J, Choi H J, Sim H H, Park B O and Ray S S 2011 Magnetic carbonyl iron suspension with organoclay additive and its magnetorheological properties *Colloids Surf. A* **377** 103–9
- [24] Bica I, Anita E M, Averis L M E and Bunoiu M 2015 Magnetodielectric effects in composite materials based on paraffin, carbonyl iron and graphene *J. Ind. Eng. Chem.* **21** 1323–7
- [25] Sahin H, Wang X and Gordaninejad F 2009 Temperature dependence of magnetorheological materials *J. Intell. Mater. Syst. Struct.* **20** 2215–22
- [26] Bahiuddin I, Mazlan S A, Shapiai I, Imaduddin F, Ubaidillah and Choi S-B 2018 Constitutive models of magnetorheological fluids having temperature-dependent prediction parameter *Smart Mater. Struct.* **27** 095001
- [27] Arief I, Sahoo R and Mukhopadhyay P K 2016 Effect of temperature on steady shear magnetorheology of CoNi microcluster-based MR fluids *J. Magn. Magn. Mater.* **412** 194–200
- [28] Wiehe A, Kieburg C and Maas J 2013 Temperature induced effects on the durability of MR fluids *J. Phys.: Conf. Ser.* **412** 012017

- [29] Bica I 2006 The influence of temperature and of a longitudinal magnetic field upon the electrical conductivity of magnetorheological suspensions *Physica B* **371** 145–8
- [30] Singh H, Singh Gill H and Sehgal S S 2016 Synthesis and sedimentation analysis of magneto rheological fluids *Indian J. Sci. Technol.* **9**
- [31] Roupoc J, Mazurek I, Strecker Z and Klapka M 2013 The behavior of the MR fluid during durability test *J. Phys.: Conf. Ser.* **412** 012024
- [32] El Wahed A K and McEwan C A 2011 Design and performance evaluation of magnetorheological fluids under single and mixed modes *J. Intell. Mater. Syst. Struct.* **22** 631–43
- [33] Hong S R, Wereley N M, Choi Y T and Choi S B 2008 Analytical and experimental validation of a nondimensional Bingham model for mixed-mode magnetorheological dampers *J. Sound Vib.* **312** 399–417
- [34] Yazid I I M, Mazlan S A, Kikuchi T, Zamzuri H and Imaduddin F 2014 Design of magnetorheological damper with a combination of shear and squeeze modes *Mater. Des.* **54** 87–95
- [35] Parlak Z, Engin T and Çalli I 2012 Optimal design of MR damper via finite element analyses of fluid dynamic and magnetic field *Mechatronics* **22** 890–903
- [36] Trilok G and Gnanasekaran N 2021 Numerical study on maximizing heat transfer and minimizing flow resistance behavior of metal foams owing to their structural properties *Int. J. Therm. Sci.* **159** 106617
- [37] Wang D, Zi B, Zeng Y, Hou Y and Meng Q 2014 Temperature-dependent material properties of the components of magnetorheological fluids *J. Mater. Sci.* **49** 8459–70
- [38] Gurubasavaraju T M, Kumar H and Arun M 2017 Optimisation of monotube magnetorheological damper under shear mode *J. Braz. Soc. Mech. Sci. Eng.* **39** 2225–40
- [39] Krishna H, Kumar H and Gangadharan K 2017 Optimization of magnetorheological damper for maximizing magnetic flux density in the fluid flow gap through FEA and GA approaches *J. Inst. Eng. Ser. C* **98** 533–9
- [40] Shivaram A C and Gangadharan K V 2007 Statistical modeling of a magnetorheological fluid damper using the design of experiments approach *Smart Mater. Struct.* **16** 1310–4
- [41] Cheng H, Hong W and Liu C 2014 Study on preparation and thermal conductivity of high stability magnetorheological fluids *J. Chin. Adv. Mater. Soc.* **2** 130–7
- [42] Mistik S I, Shah T, Hadimani R L and Siories E 2012 Compression and thermal conductivity characteristics of magnetorheological fluid-spacer fabric smart structures *J. Intell. Mater. Syst. Struct.* **23** 1277–83
- [43] Breese' D G and Gordaninejad F 1999 Heating of magneto-rheological fluid dampers: a theoretical study *Proceedings of the SPIE* **3671** 2–10
- [44] McKee M, Gordaninejad F and Wang X 2018 Effects of temperature on performance of compressible magnetorheological fluid suspension systems *J. Intell. Mater. Syst. Struct.* **29** 41–51
- [45] Wang N, Liu X, Królczyk G, Li Z and Li W 2019 Effect of temperature on the transmission characteristics of high-torque magnetorheological brakes *Smart Mater. Struct.* **28** 057002
- [46] Kumbhar B K, Patil S R and Sawant S M 2015 Synthesis and characterization of magnetorheological (MR) fluids for MR brake application *Eng. Sci. Technol. Int. J.* **18** 432–8
- [47] Nguyen Q-H and Choi S-B 2009 Optimal design of a vehicle magnetorheological damper considering the damping force and dynamic range *Smart Mater. Struct.* **18** 015013
- [48] Weiss K D and Duclos T G 1994 Controllable fluids: temperature dependence of post-yield properties *Int. J. Mod. Phys. B* **08** 3015–32
- [49] Guerrero-Sanchez C, Ortiz-Alvarado A and Schubert U S 2009 Temperature effect on the magnetorheological behavior of magnetite particles dispersed in an ionic liquid *J. Phys.: Conf. Ser.* **149** 012052
- [50] Mangal S K and Kumar A 2015 Geometric parameter optimization of magnetorheological damper using design of experiment technique *Int. J. Mech. Mater. Eng.* **10** 1–9
- [51] Nguyen Q-H, Han Y-M, Choi S-B and Wereley N M 2007 Geometry optimization of MR valves constrained in a specific volume using the finite element method *Smart Mater. Struct.* **16** 2242–52
- [52] Pavić Z and Novoselac V 2016 Notes on TOPSIS method *International Journal of Research in Engineering and Science* **1** 5–12
- [53] Dogruoz M B, Wang E L, Gordaninejad F and Stipanovic A J 2003 Augmenting heat transfer from fail-safe magneto-rheological fluid dampers using fins *J. Intell. Mater. Syst. Struct.* **14** 79–86
- [54] Xu Z-D, Sha L-F, Zhang X-C and Ye H-H 2013 Design, performance test and analysis on magnetorheological damper for earthquake mitigation *Struct. Control Health Monit.* **20** 956–70
- [55] Chooi W W and Oyadji S O 2008 Design, modelling and testing of magnetorheological (MR) dampers using analytical flow solutions *Comput. Struct.* **86** 473–82
- [56] Elsaady W, Oyadji S O and Nasser A 2021 Study of failure symptoms of a single-tube MR damper using an FEA-CFD approach *J. Intell. Mater. Syst. Struct.* **32** 1391–419
- [57] Guo P, Xie J and Guan X 2019 A thermodynamically enhanced mechanical model to study the significant effect of air variation/transport on dynamic performances of magnetorheological dampers *Proc. Inst. Mech. Eng. C* **233** 160–72
- [58] Bharathi Priya C and Gopalakrishnan N 2019 Experimental investigations of the effect of temperature on the characteristics of MR damper *Lecture Notes in Civil Engineering* vol 12 (Berlin: Springer) pp 435–43
- [59] Patel D M and Upadhyay R V 2018 Predicting the thermal sensitivity of MR damper performance based on thermo-rheological properties *Mater. Res. Express* **6** 015707
- [60] Bharathi Priya C and Gopalakrishnan N 2019 Temperature dependent modelling of magnetorheological (MR) dampers using support vector regression *Smart Mater. Struct.* **28** 025021
- [61] Du C, Zeng F, Liu B and Fu Y 2021 A novel magnetorheological fluid damper with a heat insulation function *Smart Mater. Struct.* **30** 075001